Catalysis Science & Technology

ROYAL SOCIETY OF CHEMISTRY

REVIEW

View Article Online
View Journal | View Issue

Cite this: *Catal. Sci. Technol.*, 2024, **14**, 1428

A critical review on black phosphorus mediated Z-scheme heterojunctions: properties, synthesis, and mechanistic insights towards solar H_2 evolution

Rasan Kumar Giri, Sriram Mansingh, Newmoon Priyadarshini, Jayashree Panda and Kulamani Parida *

Over the past few decades, the application of semiconductor-driven photocatalysis has emerged as an emerging tactic addressing the growing sustainable energy demands. A significant advancement in this field involves the utilization of two-dimensional black phosphorus (2D BP) as a potential metal-free photocatalyst that offers distinct advantages, including a tunable band gap (depending on the number of layers), high charge mobility, broad light absorption, substantial surface area, and specific anisotropic structure, which has gathered significant attention. This review initially documented the inherent characteristics, mostly physicochemical, optoelectronic, and catalytic properties, assessing their viability as metal-free photocatalysts. This review also provides an overview of advanced fabrication methods for various dimensional configurations of BP, *i.e.*, three-dimensional (3D) bulk, 2D nanosheets (2D NSs), and zero-dimensional quantum dots (0D QDs). Afterward, various strategies to enhance the stability of BP are also discussed in detail. The study also compiles various developments towards Z-scheme heterostructures and underlying catalytic mechanisms for boosting high photocatalytic H_2 evolution activity. Finally, challenges and future prospects in BP research are also discussed, highlighting its possibilities as a versatile material in the post-graphene era. We believe that this review may open up a new avenue for the research community toward sustainable generation of solar fuel using metal-free photocatalysts.

Received 4th November 2023,
Accepted 23rd January 2024

DOI: 10.1039/d3cy01532g

rsc.li/catalysis

Centre for Nano Science and Nano Technology, Siksha 'O' Anusandhan (Deemed to be University), Bhubaneswar 751 030, Odisha, India.
E-mail: kulamaniparida@soa.ac.in, kulamaniparida@yahoo.com

1. Introduction

The rise of global industrialization and population[1,2] has led to excessive utilization of traditional fossil fuels like

Rasan Kumar Giri

Mr. Rasan Kumar Giri has completed his M. Sc. Degree from College of Basic Science and Humanities, OUAT, Bhubaneswar. Currently, he is pursuing Ph.D. at Centre for Nano Science and Nano Technology, S'O'A (Deemed to be University) under the supervision of Prof. Kulamani Parida. His research area primarily focuses on the design and development of phosphorus modified systems for various photocatalytic applications towards energy and environment sustainability (H_2O_2 production, H_2 generation, and pollutant deprivation).

Sriram Mansingh

Dr. Sriram Mansingh received his B.Sc (2 Rank), M.Sc. and M. Phil (1 Rank) from Utkal University, India. After completed his Ph.D. degree from the Siksha 'O' Anusandhan (Deemed to be University) Bhubaneswar, India. He joined as a Tenured Faculty in the same group CNSNT. His current research mainly focuses on the development of nanostructured functional materials, such as metal oxides, metal sulphides, phosphides, and layered materials, and their application towards water splitting, N_2/O_2 reduction and organic/inorganic pollutant detoxification.

petroleum, coal, and natural gases, which propelled worldwide concerns about energy scarcity and environmental pollution.[3,4] Therefore, it is of the highest priority to scrutinize, develop, and promote an eco-friendly, carbon-neutral, and economically viable energy technology while keeping environmental protocols intact. In this context, semiconductor-based photocatalysis (artificial photosynthesis, AP) has gathered tremendous research interest as a practical way to address energy and environmental challenges.[5–7] AP is an emerging technology that effectively transfers solar energy to storable, transferable, and consumable chemical fuel for a sustainable society.

Moreover, extensive research has proven the potential use of semiconducting photocatalysts for water-splitting reactions generating H_2 fuel, offering a promising solution to the challenge posed by fossil fuels and the conventional stream reforming H_2 process.[8–10] In recent times, substantial progress has been achieved in the arena of photocatalysis, leading to the discovery of several valuable catalytic systems based upon metal oxides,[11,12] metal sulphides,[13,14] metal nitrides,[15,16] graphitic carbon nitride (g-C_3N_4),[17–19] Bi-derived materials,[20–22] metal–organic frameworks (MOFs),[23–25] and perovskite systems.[26] Still, the designed systems are associated with particular bottlenecks like a wide band gap, narrow photon absorption range, faster carrier recombination, unsatisfactory band edge potential, *etc.*, limiting the potential towards photocatalysis. Hence, it is reasonable to conduct in-depth studies on narrow band gap materials with feasible band edge alignment to determine the suitable semiconductor for the application. In this regard, 2D materials are the best candidates with unique physio-chemical and optoelectronic features.

Among many, BP, discovered by Bridgman in 1914, remained relatively overlooked for nearly a century.[27] Nevertheless, in recent times, it has emerged as a powerful nanomaterial in photocatalysis for its diverse applications towards energy and the environment, owing to its unique

Newmoon Priyadarshini

Ms. Newmoon Priyadarshini received her M.Sc. degree from Ravenshaw University. Then after she joined the Indian Institute of Technology Bhubaneswar, Odisha as JRF. Currently, she is pursuing Ph.D. at the Centre for Nano Science and Nano Technology, S'O'A (Deemed to be University) under the supervision of Prof. Kulamani Parida. Her research area focuses on the design and fabrication of single-crystal-based functional materials in the form of active pharmaceutical co-crystals, ionic liquids, MOFs, and perovskites, and their potential application in biomedical engineering, environmental pollution abatement, energy generation (piezophotocatalysis), and storage.

Jayashree Panda

Jayashree Panda received her postgraduate degree in Applied Chemistry from Central University of Jharkhand, Ranchi, Jharkhand, in 2015. Since January 2022, she has started working as a research scholar under the supervision of Prof. Kulamani Parida at Centre for Nanoscience and Nanotechnology, S'O'A deemed to be University, Bhubaneswar, Odisha, India. Her current research interests are focused on the design of functionalized MOFs and MOF derived nanomaterials towards emerging photocatalytic applications.

Kulamani Parida

Prof. Kulamani Parida is a globally distinguished scientist in the areas of Materials Science, Catalysis and Nanotechnology. He superannuated as a Chief Scientist and a Professor of Academy of Scientific and Innovative Research (AcSIR) from CSIR-IMMT, Bhubaneswar in 2014. His adoration for Chemistry and passion for research couldn't let Prof. Parida to sit idle after retirement. With the same devotion and dedication, Prof. Parida (Director) started the 'Centre for Nano Science and Nano Technology' a research unit of Siksha 'O' Anusandhan (deemed to be university), Bhubaneswar. His research interests include the design and development of advanced materials encompassing fine chemical, energy generation/storage, and environmental applications. He has published more than 485 research articles and review articles in renowned international journals. He bags a citation of 31481 to his credit with h-index of 95 and i10-index of 426. He has featured in the global 2% scientist list for the last three consecutive years. For more details: **https://kmparidaimmt.weebly.com/**

inherent qualities.[28–31] One remarkable feature is its ability to exfoliate into 2D NS and 0D QD structures through the weaker interlayer interaction (van der Waals forces) found in 3D bulk BP, resulting in a significant enhancement of catalytic efficiency.[32,33] BP exhibits significant optical absorbance across the visible to near-infrared (NIR) spectrum and possesses a directly tunable band gap, with a variation between 0.3 and 2.0 eV, transitioning from bulk BP to monolayer BP.[34] Moreover, the high charge carrier mobility, specific crystal framework, and electrical solid conductivity further enhance its suitability as an exceptional photocatalyst.[35,36]

Furthermore, BP also holds great potential for H_2 production. However, its inherent instability prevents its practical implementation. In brief, each P atom inside the folded honeycomb BP lattice structure is coupled with a neighbouring P atom, where the unshared electron pair of P interacts through both oxygen and water, enabling BP to be extremely reactive.[37] In most cases, the non-bonded electron pair of P interacts with oxygen in the atmosphere, producing oxides of P, *i.e.*, P_xO_y. Consequently, water molecules associate with P_xO_y through H-bonding, disrupting the BP network structure. As a result, the practical utility of BP is hindered due to its reactivity and, subsequently, loss of its semiconductor properties.[38,39] However, Ji *et al.* (2017) were the first to report H_2 evolution over BP NSs,[40] but the catalytic efficiency was lower compared to many reported 2D photocatalytic systems, including $ZnIn_2S_4$,[41] TiO_2,[42] g-C_3N_4,[43] CdS,[44] *etc.* The low catalytic activity of BP may be attributed to (i) the faster recombination of photo-produced excitons, which hinders their efficiency as photocatalysts, and (ii) upon exposure to air, water, and light, BP-based materials exhibit limited chemical stability.[45–48] Hence, there is a significant demand for developing a durable and efficient BP-based photocatalytic H_2 evolution catalyst. Moreover, it is possible to solve the above-discussed limitations by adopting various modification techniques, including doping, defect engineering, heterojunction formation with other semiconductors, noble metal loading, forming a composite with carbonaceous materials, *etc.*

To address these challenges, researchers have developed a stable internal electric field (IEF) that allows BP to interact with various photocatalysts by constructing suitable heterostructures. Generally, heterojunctions can be categorized as either p–n or n–n types depending on specific semiconductors involved in various photocatalytic activities. The development of a built-in electric field in the case of p–n type heterojunctions[49–52] and the migration of free electrons in n–n type heterojunctions[53] are the influential factors that trigger the segregation of excitons, enhancing photocatalytic responses. In this context, Zhu *et al.* (2017) and Wen *et al.* (2019) designed a type-I heterostructure by integrating BP with g-C_3N_4 for H_2 evolution.[54,55] Song *et al.* (2019), Lei *et al.* (2018), Ran *et al.* (2017), and Elbanna *et al.* (2019) designed BP-based type-II heterostructures with BP/3D reticulated carbon nitride (CN), BP QDs/g-C_3N_4 hybrids, $Zn_xCd_{1-x}S$/BP and BP/TiO_2, respectively.[56–59] These heterojunctions aid in the efficient spatial segregation of charges, allowing for the effective conveyance of photoexcited electron–hole (e^-–h^+) pairs.[60–62] Additionally, constructing heterojunctions with solid chemical bonds can improve the stability of BP photocatalysts.[54,63] Despite the current efforts in developing composite heterojunctions based on BP photocatalysts, there remains a lack of extensive studies that explore the various applications of heterostructures based on BP across multiple disciplines. Therefore, a unique heterojunction, *i.e.*, Z-scheme heterojunction, came into practice, which maintains a greater redox potential that restricts the recombination of excitons for enhanced photocatalytic activity.[64] Further, Z-scheme based heterojunction systems are more effective than double charge transfer (DCT) oriented systems toward H_2 generation. In DCT mode, the overall redox potential of the heterojunction decreases; however, in the Z-scheme charge transfer (CT) route, the highly oxidising holes and highly reducing electrons are retained, resulting in high catalytic performance (discussed in detail in a later section). Additionally, noticeable advancement has been achieved in BP-based systems towards the H_2 evolution reaction, but no such review highlights H_2 production on BP-oriented photocatalysts, mainly *via* Z-scheme charge dynamics.

This review describes a concise layout of various critical features of BP-mediated photocatalysts, including their structural aspects related to crystal and band structures along with optical, electrical, and thermal properties. Afterward, we delivered standard methods for fabricating BP in various dimensional configurations, like 3D bulk structure, 2D NSs, and 0D QDs. In the third section, we discussed various techniques to enhance the stability of BP in detail as well as the fundamentals and associated mechanisms regarding Z-scheme heterostructures. In the last section, we have mentioned the critical features of recently reported various Z-scheme based BP systems for photocatalytic H_2 evolution. Finally, we wrapped up the review by presenting some individual viewpoints on the current problems and possible forthcoming research pathways of BP-based Z-scheme heterojunction photocatalysts.

2. Properties of black phosphorus

2.1 Crystal structure

Generally, BP exists in mainly three crystallographic phases, *i.e.*, orthorhombic, hexagonal, and cubic. At standard temperature and pressure, BP exists in the orthorhombic phase, but at high pressure, it undergoes a phase transformation into the hexagonal (5 GPa) and cubic (10 GPa) phases, respectively.[65] Similarly, under a pressure of 5 GPa, the orthorhombic phase of BP transitions into the rhombohedral phase.[66,67] Bulk BP, as illustrated in Fig. 1a, comprises multiple monolayer BP units that are bonded together by van der Waals forces, resulting in a layer separation distance of 5.3 Å.[68] Additionally, monolayer BP

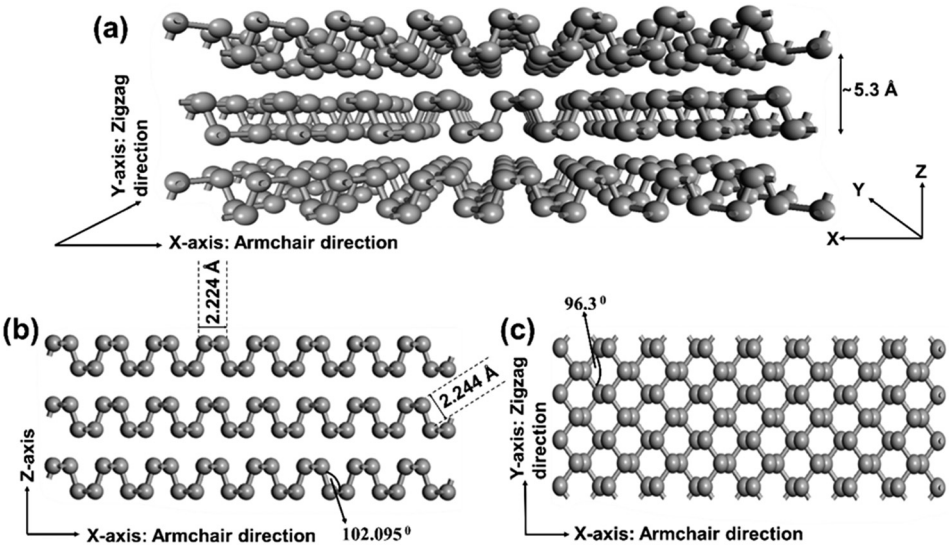

Fig. 1 Schematic layered BP crystal structure representation. (a)–(c): 3D view top view, and side view, respectively (P atoms represented by grey balls). Adapted with permission.[71] Copyright 2015, Royal Society of Chemistry.

has a wrinkled honeycomb structure due to the covalent bond between each P-atom and nearby three P-atoms and also because of sp^3 hybridization between the P-atoms. The two bond angles that BP obtained from this wrinkled structure were 96.300° (Fig. 1b) and 102.095° (Fig. 1c), both of which are almost as big as the angle in the tetrahedron arrangement (109.5°). The top and bottom P-atoms in monolayer BP have a bond length of 2.244 Å. On the other hand, the P-atoms adjacent to each other within the same plane exhibit a bond distance of 2.224 Å (Fig. 1b). Moreover, BP exists in armchair and zigzag mode of arrangements along the *x*- and *y*-axis, respectively (Fig. 1a and c). Furthermore, the exceptional electrical, optical, and thermal anisotropy that BP displays along the two dimensions makes it more versatile than other 2D materials in photocatalytic applications. Further, BP materials are highly receptive to air and moisture, causing degradation of the framework and significant variation in properties related to crystal structure. Therefore, it is crucial to emphasize that modifying the pressure on BP can lead to a change in its crystal structure. These alterations in the crystal structure significantly impact various properties of BP, particularly affecting the band gap and various optical properties.[69,70] Additionally, it is worth noting that variations in pressure can also influence the fabrication of BP nanomaterials, as elaborated in detail in section 3.1.1.

2.2 Band gap framework

The band gap framework is the most fundamental essential parameter in photocatalytic processes using semiconductors. In this regard, BP is used significantly for the variable band gap structure as a photocatalyst. Hence, it is essential to identify the optical band gap and band edge position of photocatalysts based on BP. Keyes (1953) identified a band gap of 0.33 eV in bulk BP.[72] However, research on BP, specifically the determination of the band gap and its energy levels, has been delayed for almost six decades due to difficulties in fabricating bulk BP and a lack of sophisticated characterisation methods. Tran *et al.* (2014) employed theoretical calculations to determine a band gap of approximately 0.3 eV in bulk BP, aligning closely with the experimental finding of Keyes, *i.e.* 0.33 eV.[73] Subsequent research, based on both theoretical calculations and experimental outcomes, proposed modifications to the band gap of BP in both bulk BP and few-layer BP (FL BP).[74–79] However, achieving precise results remains an ongoing challenge. In this regard, Rudenko *et al.* attempted to estimate the approximate band gap of bulk BP using the GW approximation method and reported a value of 0.1 eV.[74] While this value wasn't particularly high, the research team anticipated that achieving self-consistency in the G and W calculations would lead to an increase in this value. The team utilized the results for determining the band structure of monolayer phosphorene to four-layer phosphorene (Fig. 2a), which revealed that, with an increase in the number of phosphorene layers, the band gap also increased. To describe the band energy of the orbital configuration, they additionally projected the GW quasiparticle states onto the conventional s-orbitals and p-orbitals. However, due to the involvement of s-orbitals and p-orbitals (p_X and p_Z orbital), the formation of the valence-band (VB) and conduction-band (CB) without the participation of the p_Y orbital occurs. Additionally, in comparison to the band gap of graphite, which solely depends upon the p_Z orbital, the band gap framework of BP is more condensed due to the asymmetry provided by the mixed phase.

Furthermore, in recent years, along with theoretical calculations, researchers also frequently adopted experimental techniques like PL and UV-DRS analysis to calculate the band gap of BP. Based on the analysis of PL

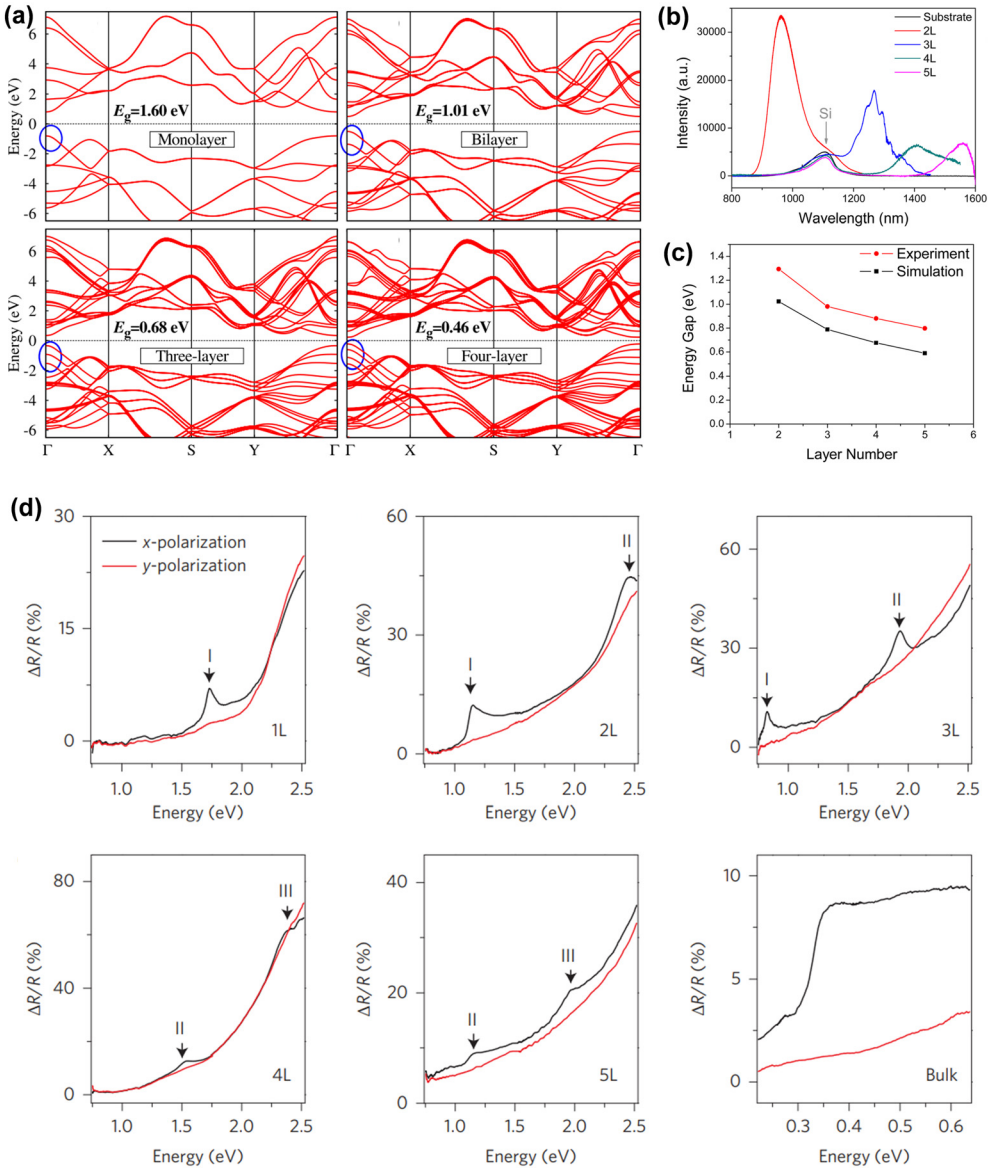

Fig. 2 (a) The variation of band gap for phosphorene layers (1–4 layers) using the GW approximation method. The zero energy at the centre of the band gap is illustrated by the blue circles. Adapted with permission.[74] Copyright 2014, American Physical Society; (b and c) PL spectra and energy gap of simulated and experimental PL spectra of 2, 3, 4 and 5 L phosphorene, respectively. Adapted with permission.[75] Copyright 2014, American Chemical Society. (d) Band gaps of 1 L, 2 L, 3 L, 4 L, 5 L phosphorene and bulk BP using reflection spectra. Adapted with permission.[76] Copyright 2016, Nature Publishing Group.

spectra and observation of the band gaps (2, 3, 4, and 5 layered BP), Zhang and colleagues concluded that adding phosphorene layers decreased the band gap of BP (Fig. 2b), which remains consistent with their theoretical calculations (Fig. 2c).[75] In a similar manner, Li and colleagues calculated the energy band gaps for bulk BP and phosphorene sheets consisting of 1, 2, 3, 4, and 5 layers using reflection spectra, as depicted in Fig. 2d.[76] Therefore, the band gap was determined for both bulk BP and different phosphorene layers using theoretical calculations and experimental findings, with a tendency for the band gap to rise with a decrease in thickness. Additionally, the band gap of BP may be modified externally using techniques like doping,[80] producing an external electric field,[81] and strain engineering.[82] Moreover, although BP has a narrow band gap, *i.e.* 0.3 eV, it is utilized as a cocatalyst with TiO_2 and MoS_2.[83,84] However, bulk BP is limited to photocatalytic hydrogen evolution reactions (HER) owing to the rapid recombination of photo-produced charge carriers. Therefore, the tunable bandgap makes a broad impact on the photocatalytic application. For instance, Zou *et al.* (2018) introduced a 2D–2D BP/MoS_2 heterojunction for enhanced photocatalytic H_2 production of about 1286 μmol h^{-1} g^{-1} *via* the liquid-phase exfoliation (LPE) method.[85] The team observed that the transformation of bulk BP (band gap of 0.3 eV) into few-layered black

phosphorus nanosheets (FL BP NSs) (band gap varied from 0.77 eV to 1.32 eV) resulted in enhanced photocatalytic activity owing to the formation of heterostructure with MoS_2. Hence, the team concluded that the enhanced photocatalytic H_2 production of BP NSs is owing to a decrease in the number of layers of BP using MoS_2 as a co-catalyst. Likewise, Zhu *et al.* (2017) demonstrated that when exposed to visible light without the assistance of any noble metal co-catalyst, the rate of photocatalytic H_2 production for BP NSs reached approximately 512 μmol h^{-1} g^{-1}, nearly 18 times greater than that of bulk BP.[40]

2.3 Anisotropy

A material is considered to be anisotropic when variations in its physical properties are observed based on different crystal orientations. In the case of BP, the in-plane anisotropy can be achieved by modifying the bond lengths and angles across the orthogonal plane of BP.[86,87] This structural anisotropy in

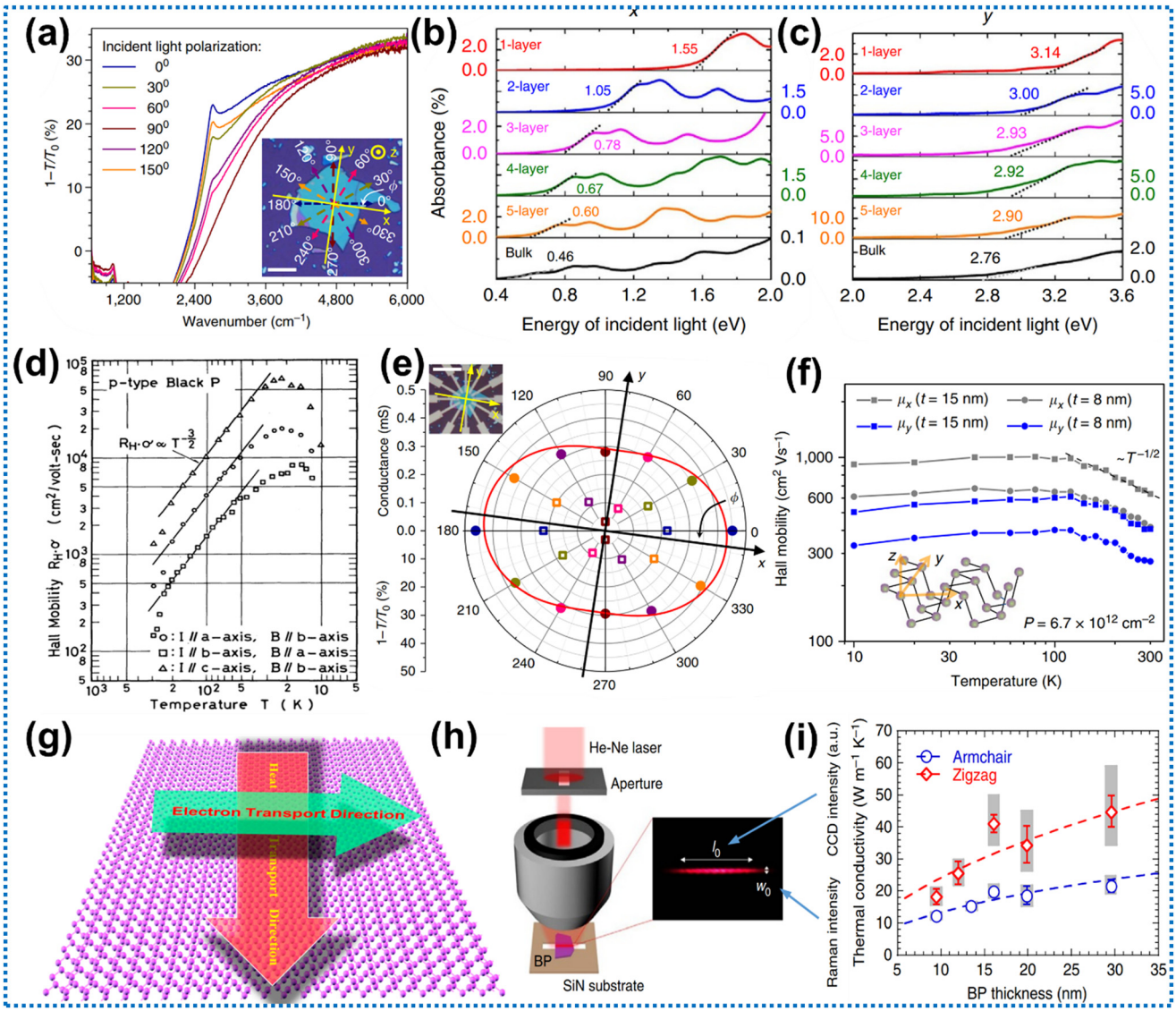

Fig. 3 (a) Diagrammatic illustration of a decrease in intensity, when polarized light was directed towards the IR region along the armchair (*x*-axis) pathway, demonstrating the thickness of BP, which was around 30 nm. Adapted with permission.[92] Copyright 2014, Nature Publishing Group; (b and c) optical absorption spectra of FL BP when light is incident along the *z*-axis and polarized along the armchair (*x*-axis) and zigzag (*y*-axis) orientations, respectively. Adapted with permission.[77] Copyright 2014, Nature Publishing Group; (d) the Hall mobilities of bulk BP, varied with temperature in the zigzag (a), out-of-plane (b), and armchair (c) directions. Adapted with permission.[86] Copyright 1983, The Physical Society of Japan; (e) DC conduction measurement and comparative IR extinction in polar coordinates along six directions; (f) angle-resolved Hall mobility measurement at a constant concentration of hole doping. Adapted with permission.[92] Copyright 2014, Nature; (g) monolayer phosphorene displaying orthogonal electrical and thermal conductivity. Adapted with permission.[95] Copyright 2014, American Chemical Society; (h) an optical representation of the laser focal line generated and the experimental apparatus; (i) thermal conductivities in the armchair and zigzag (in-plane) directions of various BP films. Adapted with permission.[97] Copyright 2014, Nature Publishing Group.

BP enables the possibility of in-plane optical, electrical, thermal, mechanical, and vibrational anisotropy in both the *x*-axis and *y*-axis.[88] Consequently, these unique features of BP are utilized by researchers for the development of several innovative optoelectronic components and can also influence the photocatalytic efficiency of the system.

2.3.1 Optical anisotropy. Optical anisotropy is a property of a material or medium where the optical properties, such as absorbance and refractive index, depend on the direction of propagation or polarization of light. In other words, the material exhibits different optical properties along different axes or directions. The optical anisotropy of thin-layer BP may be explained by the polarization-induced absorption of light,[89,90] transmission of light,[89] and reflection of light.[76,91] In this context, Xia and his teammates in ref. 92 explained the thickness of BP, (30 nm), using infrared (IR) spectroscopy. This discovery demonstrated that the polarised light experienced a significant degree of extinction in the armchair path under the effect of the IR region, as shown in Fig. 3a.[92] Qiao *et al.* investigated the photon absorption spectra of bulk BP and FL BP by varying the wavelengths of polarized light and using the dielectric function.[77] Furthermore, it was also observed that the light absorption tendency on both the *x* and *y* axes gradually reduced with an increase in the number of dielectric polarizations, as shown in Fig. 3b and c. The armchair orientation was more beneficial for the harvesting polarised light, as verified by the fact that the armchair path decreased more rapidly, and the light that was polarised in a zigzag pattern had a higher energy absorption edge. In the investigation by Ling *et al.*, it was discovered that, particularly at about 9 nm thickness and 225 nm thickness of BP, it successfully absorbed polarised light along the armchair pathway.[90] These theoretical calculations and empirical observations demonstrated the relationship between crystallographic orientation and the absorbance of light by BP. Further studies carried out by He *et al.* revealed that the proportion of light absorbance along the *x*-axis was ten times higher compared to that along the *y*-axis.[93] Moreover, the photocatalytic process, which depends on photo-excited e^-–h^+ carriers, was significantly impacted because the armchair trajectory has a 16 times better photon diffusion than the zigzag path.

2.3.2 Electrical anisotropy. BP exhibits remarkable electrical anisotropy due to the variation in effective masses of excitons moving along the zigzag and armchair path. In 1983, Akahama *et al.* utilized the multidimensional Hall effect to assess the conductivity and mobility of carriers in bulk BP. From their findings, it was observed that the mobility of charge carriers of BP towards the armchair direction was outstanding compared to zigzag orientations, as depicted in Fig. 3d.[86] Subsequent research demonstrated that not only mobility but also the conductivity of charge carriers of FL BP is highest across the *x*-axis, in contrast to the *y*-axis (Fig. 3e and f).[92] Moreover, Qiao *et al.* also provided a theoretical explanation stating that the mobility of electrons in a single-layer phosphorene about the *x*-axis was 1100–1140 $cm^2\ v^{-1}\ s^{-1}$, a substantial 14 times higher compared to the *y*-axis, approximately 80 $cm^2\ v^{-1}\ s^{-1}$. However, the mobility of holes across the *y*-axis varied between 10 000 and 26 000 $cm^2\ v^{-1}\ s^{-1}$, which marked a substantial 40 times increase compared to the *x*-axis (ranging approximately from 640 to 700 $cm^2\ v^{-1}\ s^{-1}$).[77] The remarkable mobility of BP has a substantial impact on the transmission of charge carriers. In summary, both computational and experimental results offer strong evidence for the electrical anisotropic behaviour of BP.

2.3.3 Thermal anisotropy. Riedner and team (1979) made a significant discovery about bulk BP by revealing that its thermal expansion coefficient is higher across the *x*-axis, highlighting the thermal anisotropy of BP.[94] Additionally, Fei *et al.* (for the first time) employed theoretical calculations to investigate the in-plane thermoelectric properties of single-layer BP.[95] They found that the in-plane thermal conductivity across the *y*-axis was significantly higher than that of the *x*-axis, which contradicted the result of electrical conductivity, primarily oriented along the *x*-axis (Fig. 3g). Based on the findings of Fei *et al.*, Jain and team reported that at room temperature (RT) the heat-transmission efficiency of BP along the *y*-axis was about 110 $W\ m^{-1}\ K^{-1}$, almost three times that across the *x*-axis *i.e.*, 36 $W\ m^{-1}\ K^{-1}$.[96] Using micro-Raman technology, Luo and team estimated the heat-transmission efficiency of FL BP having a thickness between 9 and 30 nm (Fig. 3h).[97] The experimental findings demonstrated the thickness-dependent anisotropic variations in heat-transmission efficiency of BP NSs, which vary from 10–20 $W\ m^{-1}\ K^{-1}$ about the *x*-axis and 20–40 $W\ m^{-1}\ K^{-1}$ across the *y*-axis (Fig. 3i). Lee *et al.* also observed the heat-transmission efficiency of BP NSs with a thickness about 170 nm, 270 nm, and 310 nm.[98] Furthermore, studies and results related to the thickness of BP have indicated that BP with only a few layers or in an ultrathin form exhibits limited heat conduction efficiency, primarily resulting from the thin-layer BP lattice from crystal scattering. As a result, BP possesses promising applications in thermoelectric devices due to its unique characteristics of thermal and electrical conductivity anisotropy.

Although the catalytic activity of BP depends on its inherent characteristics, the practical utilization of BP is quite difficult despite having excellent optical and electrical properties. Therefore, several strategies have been employed to suppress the photo-produced excitons, accelerate charge carrier mobility, enhance the conductivity, increase the stability, and expose more active sites for improving the photocatalytic activity of BP. To overcome these limitations some techniques have been adopted, which include the stability of BP (as discussed in section 4) and forming an appropriate heterojunction with a special focus on the Z-scheme type CT mechanism (detailed explanation in section 6). Since the photocatalytic reactions occur on the surface, the exposed crystal facets significantly influence the reactivity and efficiency of photocatalysis. Hence, intentionally designing a morphology that exposes highly reactive facets with superior activity requires careful

consideration. In this context, Hu *et al.* (2016) for the first time confirmed that among different morphologies of BP, *i.e.* 3D bulk BP, 2D BP NSs, and 0D BP QDs, 2D BP can serve as an excellent photocatalyst for the conversion of solar energy into chemical energy.[99] Furthermore, scientists also proved that as compared to bulk BP, ultrathin phosphorene is considered to be a potential photocatalyst that can produce $^1O_2$ (singlet oxygen) and $^{\cdot}OH$ (hydroxyl radicals) under the irradiation of UV-vis light.[100,101] Recent progress indicates that decreasing the thickness or size of BP results in the exposure of additional active sites, facilitating adsorption and desorption processes.[102] Hence, FL BP is widely recognized as a semiconductor abundant in active sites crucial for catalytic processes such as adsorption, activation, and reactions in the catalysis field.[103] It inherently exhibits catalytic activity and can serve as a co-catalyst alongside g-C_3N_4 and other catalysts that are comparatively inert.[54] The above-mentioned examples suggest that BP exhibits enhanced photocatalytic performance when the bulk form of BP is reduced into FL BP. Therefore, based on the facts discussed for the anisotropic behaviour of BP, it can be concluded that FL BP can be considered one of the most promising materials which overcome the drawbacks of transition metal dichalcogenides (TMDs) (having tunable band gap and low charge carrier mobility) and graphene (high charge carrier mobility without holding band gap) owing to its tunable band gap as well as suitable anisotropic behaviour. Therefore, phosphorene can be utilized for various applications most specifically in the field of photocatalysis.

3. Synthesis method for black phosphorus

The methods of fabrication of BP have been a quite challenging task. However, many more advanced and facile preparation techniques have been developed and followed. In this regard, Scheme 1 depicts the various synthesis methods, and the mentioned section describes the details of the procedure with suitable reported examples.

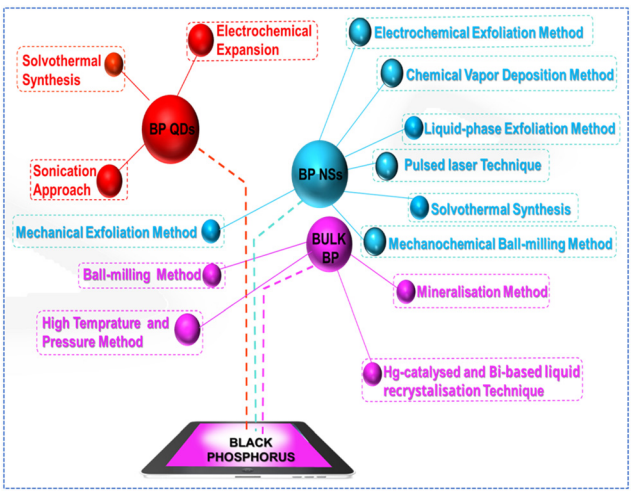

Scheme 1 Schematic representation of different adopted BP fabrication methods.

3.1 Preparation of bulk black phosphorus

BP is a unique allotrope of phosphorus (P) that has gained significant attention due to its unique properties, like band gap tunability and high carrier mobility. Synthesis of bulk BP has been carried out continuously for more than one hundred years, which involves various methods discussed as follows:

3.1.1 High temperature and pressure method. In 1914, a significant milestone was achieved by Bridgman who converted white phosphorus (WP) into bulk BP crystals for the first time. This transformation was accomplished under a hydrostatic pressure of 1.2 GPa at 200 °C operational temperature.[27] The bulk BP exhibited a density of about 2.69 kg m^{-3}, greater than the densities of commercial WP, *i.e.*, 1.83 kg m^{-3} and red phosphorus (RP), which ranges between 2.05 and 2.34 kg m^{-3}. BP exhibited excellent thermal stability as compared to both RP and WP, which didn't catch fire even at 400 °C in the presence of air. Besides, Bridgman observed a small quantity of RP and some untransformed WP in the synthesized sample, indicating impurity formation during the preparation. Furthermore, the low yield and harsh reaction conditions made this method unfavourable for practice. Bridgman, again in 1937, was able to prepare bulk BP by using RP as a precursor at RT by applying a higher pressure of about 8.0 GPa.[104] Subsequently, Keyes *et al.* (1953) successfully synthesized BP under hydrostatic pressure (2.6 GPa) and temperature (473 K) and observed an anisotropic behaviour of BP using various electrical measurements.[72] Further, Shirotani *et al.* (1982) were able to fabricate BP crystalloids having a diameter and length of 4 nm and 5 nm, respectively, by applying high-pressure (2.3 GPa) at 500 °C to WP.[105] In another work, Endo *et al.* (1982) synthesized single-crystalline BP of sizes $> 5 \times 5 \times 10$ mm^3 using RP, comparatively at low pressure (1 GPa) and elevated temperature (900 °C).[86] In summary, the process involved the production of BP by initial heating of RP to approximately 550 °C, then subjecting it to melting at 900 °C under a pressure of 1 GPa. Subsequently, the system was gradually cooled at a rate of 0.5 °C min^{-1} to 600 °C, leading to solidification, and ultimately, the desired product was obtained. Sun and team (2012) also synthesized BP from RP within a short duration of 15 min under high pressure ranging from 2 to 5 GPa and temperature within the range of 293 K to 1073 K (Fig. 4a).[106] However, these are complex methods for researchers to synthesize bulk BP inside laboratories because of the involvement of extreme experimental conditions such as high temperature or high pressure.

3.1.2 Ball-milling method. Ball milling is the technique used for synthesizing nanomaterials using mechanical energy in which phase transition takes place because of high

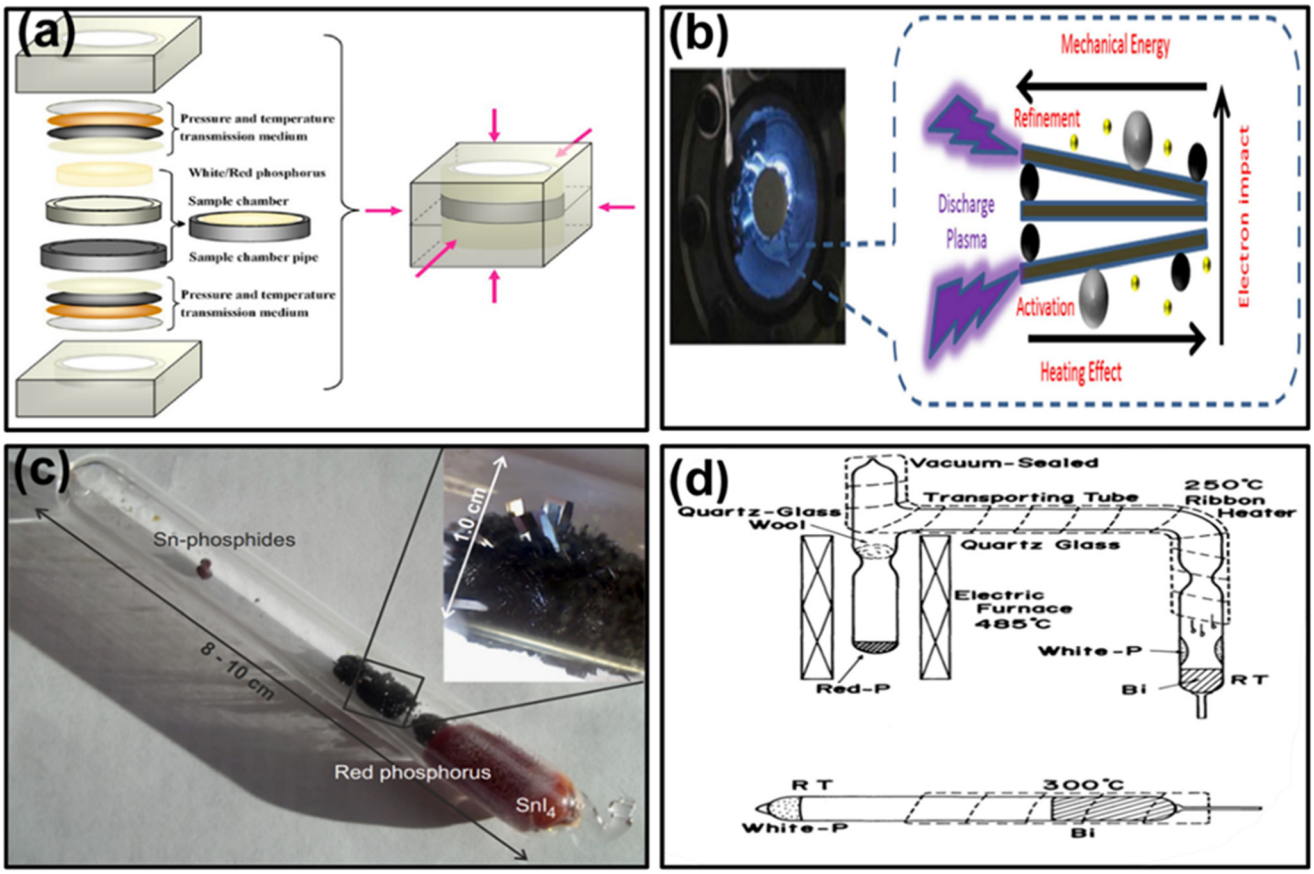

Fig. 4 (a) A diagram illustrating the arrangement carried out for the synthesis of BP. Adapted with permission.[106] Copyright 1989, American Chemical Society; (b) principle of ball milling. Adapted with permission.[107] Copyright 2017, Elsevier; (c) mineralization process for BP synthesis using a SnI_4 catalyst. Adapted with permission.[114] Copyright 2014, Elsevier; copyright 2019, Nature Materials; (d) diagram demonstrating the fabrication of BP using the Bi-flux method. Adapted with permission.[117] Copyright 1989, Japanese Journal of Applied Physics.

pressure and temperature produced by the collisions between the spheres and the wall of the vessel. A ball mill is a grinder or blender consisting of a cylindrical hollow shell that rotates around its axis where the axis appears to be horizontal or at a little angle to horizontal. The axis is partly filled with rubber, ceramic, and steel balls, such as chrome or stainless steel. In addition, the inner surface of the shell is lined with materials like rubber and manganese steel (Fig. 4b).[107] Zhou and group (2019) used three types of ball milling methods: plasma-assisted ball milling, planetary milling, and shake milling to synthesize BP. In addition, these mentioned methods operate under high mechanical energy that reduces the milling time and increases the grinding efficiency, resulting in highly crystalline BP.[108] Therefore, it can be inferred that RP transformed to BP was due to applying higher mechanical energy and generating higher pressure because of the collision between the balls and the vessel wall during ball milling methods. Subsequently, using this method, Zhang and co-workers (2018) synthesized amorphous BP as confirmed *via* microstructural characterization.[109] Here, they observed that this process consumed less energy as compared to the high-pressure method, and the yield of BP was comparatively higher. Besides, the observed BP was smaller in size, showed poor crystallinity, and had some RP residue. Similarly, Shin *et al.* (2019) also prepared BP powder using RP (precursor) by applying a high-energy mechanical milling method.[110] Park and Sohn (2007) synthesized BP using RP as the precursor by applying a temperature above 200 °C and a pressure of about 6 GPa.[111] Although the synthesized material showed poor crystallinity, it was utilized as an anodic material for rechargeable lithium-ion (Li-ion) batteries. In the same year, Lange and group synthesized BP crystals using RP, SnI_4, and AuSn as the raw materials under low pressure at 873 K.[112]

3.1.3 Mineralisation method. Compared to the above discussed synthesis methods, researchers produced massive products along with small amounts of by-products using mineralisation methods. To reduce the cost of the synthesis procedure, SnI_4 was used as a mineraliser for synthesizing BP. In 2008, Nilges and co-workers sealed RP and SnI_4 (prepared by mixing Sn powder with iodine in 25 mL of toluene) in ampoules, which were placed inside a muffle furnace at varying temperature of about 673 K to 873 K for 24 hours, producing BP.[113] Similarly, Köpf *et al.* (2014) used the same mineraliser to synthesize BP, avoiding the use of Au during synthesis, and the output

was enhanced by optimizing temperature, as shown in Fig. 4c.[114]

3.1.4 Hg-catalysed and Bi-based liquid recrystallisation technique. The mercury (Hg)-catalysed method was developed to minimize the pressure for the synthesis of BP.

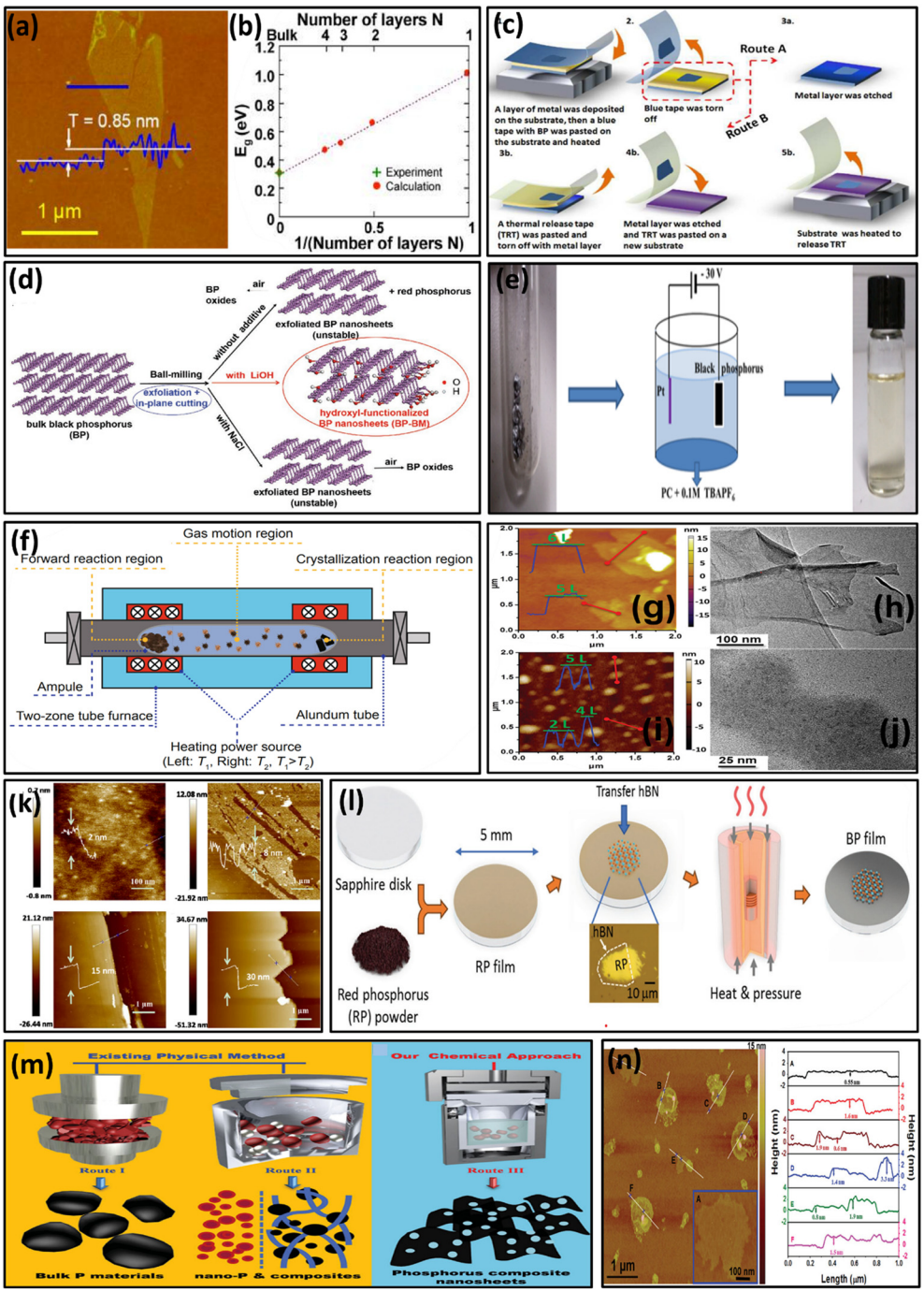

Fig. 5 (a) AFM analysis of monolayer phosphorene; (b) DFT analysis for energy gap determination in FL BP. Adapted with permission.[118] Copyright 2014, American Chemical Society; (c) metal assisted exfoliation of FL BP. Adapted with permission.[119] Copyright 2013, Royal Society of Chemistry; (d) synthesis of BP NSs using the ball milling method. Adapted with permission.[40] Copyright 2017, Wiley; (e) scheme demonstrating the synthesis of BP NSs using the electrochemical exfoliation method. Adapted with permission.[126] Copyright 2017, Wiley; (f) CVT method employed for the synthesis of BP NSs. Adapted with permission.[129] Copyright 2016, Springer; (g and i) AFM analysis of BP NS centrifugation at 12 000 and 18 000 rpm respectively; (h and j) TEM analysis of BP NS centrifugation at 12 000 and 18 000 rpm respectively.[134] Copyright 2015, Wiley; (k) AFM analysis of BP thin films. Adapted with permission.[143] Copyright 2015, Wiley; (l) schematic illustration of large-scale BP synthesis. Adapted with permission.[144] Copyright 2018, Wiley; (m) synthesis of P-based nanomaterials through solid-state (physical) and solvothermal methods (chemical); (n) AFM images with height measurements of BP NSs. Adapted with permission.[145] Copyright 2016, Wiley.

In this context, Krebs *et al.* in 1955 were able to produce BP from WP thermally using Hg as the catalyst at low pressure.[115] The observed BP crystals were contaminated by some amounts of Hg, reducing their applicability.

Afterward, Maruyama and associates (1981) synthesized single BP crystals of needles or thin rod morphology using the liquid-bismuth (Bi) recrystallisation method.[116] In this approach, commercial WP was combined with Bi in a Pyrex glass tube, which was sealed with helium (He) gas after thorough cleaning with 15% nitric acid and subsequent distillation *via* steam water. The mixture of WP and molten Bi was blended well, and the solution was maintained at 400 °C for 20 hours. After allowing it to cool down to RT, the solid Bi was dissolved in nitric acid (30%) to get BP from the solution. However, it's important to note that these methods have significant drawbacks, including their toxicity and low yield, which prevent further long-term use. Baba *et al.* (1989) used an evacuated quartz-glass apparatus to fabricate single BP crystals that resemble thin films or plates.[117] Initially, the quartz-glass ampoule was heated to 80 °C in a hot bath to melt WP (MP: 44.1 °C). The liquid WP was pushed in the opposite direction of Bi and then allowed to solidify. Subsequently, using a ribbon heater, Bi was heated to a temperature of roughly 300 °C; meanwhile, the molten Bi was put over the WP. The ampoule was then placed in an electric furnace set at 400 °C for 48 hours before being allowed to cool to 200 °C and then cooled to RT. Finally, the ampoule was broken, and the resultant lump was kept in a 30% nitric acid solution to dissolve Bi. Finally, BP crystals were fabricated from the residual solution, as shown in Fig. 4d.

3.2 Synthesis of 2D black phosphorus nanosheets

In contrast to bulk materials, 2D materials offer several advantages like planarity, greater conductivity, specific anisotropic structure, tunable band gap, substantial surface area, and broad light absorption range. Consequently, researchers have concentrated more on the development of ultrathin 2D NSs aiming at their potential use for a wide range of applications. Various techniques have been introduced for the fabrication of 2D NSs, which are elucidated below.

3.2.1 Mechanical exfoliation method. Owing to the presence of relatively weak van der Waals forces between layers of bulk BP, delamination to ultrathin 2D NSs on applying mechanical forces/stress is facile in bulk BP structure. In 2014, Liu and colleagues initiated the utilization of a Scotch-tape-based micro-cleavage technique for exfoliating layered bulk BP into single-layer, atomically thin BP NSs. These thin sheets are known as phosphorene, a p-type semiconducting material, and are characterized *via* AFM, as depicted in Fig. 5a.[118] The band gap of ultrathin NSs, which was determined to be greater than the bulk BP at approximately 0.31–0.36 eV, was described by *ab initio* calculations to be affected by the layer number and layer strain (Fig. 5b). Additionally, the PL of single-layer phosphorene in the visible region also supported the idea that it has a larger band gap than bulk BP; all these above-discussed observations confirmed the exfoliation of bulk BP. Even though good quality BP was synthesized, the low yield of BP could have been much higher. Subsequently, Xia *et al.* also exfoliated BP NSs from massive BP crystals utilizing the micromechanical cleavage technique using a 300 nm SiO_2 grid on a Si substrate.[92] Similarly, Guan and colleagues (2018) were also able to produce ultrathin BP NSs by enhancing the Si grid and using Au/Ag as a cutting sheet. The obtained BP NSs were nearly 100-fold larger in surface area and had lateral sizes over 50 μm compared with BP NSs produced using standard "scotch-tape" techniques.[119] In addition, the field effect transistor demonstrated a hole mobility of about 68.6 $cm^2\ v^{-1}\ s^{-1}$ and an on/off current, which reached nearly 2×10^5 μA cm^{-2} (Fig. 5c). In another work, Zhao *et al.* (2017), for the first time, synthesized unique 2D polycrystalline BP NSs by adopting a moderate synthetic method.[120] The team used RP as the precursor along with NH_4F to reduce the activation energy of RP. The BP NSs were synthesized on the application of phase transformation of P utilizing Gibbs free energy, which showed high photocatalytic efficiency, good electrochemical performance, and anodic function for lithium-ion batteries. Because of this, the energy sector extensively uses this new synthetic approach for designing ultrathin BP NSs.

3.2.2 Mechanochemical ball-milling method. Ball-milling is a successful mechanical exfoliation technique for producing BP NSs. Zhu *et al.* (2017) used anhydrous LiOH and bulk BP to synthesize BP NSs *via* a ball-milling method under an Ar environment, where LiOH restricted the phase alteration of RP to BP (Fig. 5d).[40] Additionally, the performed microscopy characterization illustrated that the BP NSs were between 300 and 500 nm in size and between 0.7 and 6 nm in thickness. Consequently, under the illumination of visible light without the support of any noble metal (co-catalyst), the rate of photocatalytic H_2 production of BP NSs was around 512 μmol $h^{-1}\ g^{-1}$, nearly 18 times higher than that of bulk BP.

3.2.3 Electrochemical exfoliation method. As compared to methods that can produce materials with high yields and controllable quality, such as liquid-phase exfoliation, mechanical cleavage, and the electrochemical expansion mechanism, this technique is applied for producing 2D materials *via* cationic intercalation and anodic oxidation that is primarily used to expand the structure of bulk layered materials that, when immersed in a liquid electrolyte, undergo electrochemical exfoliation in response to an externally supplied electric field. Huang *et al.* (2017) conducted an experiment where they used a solution containing electrolytes such as dimethylformamide (DMF) and tetrabutylammonium hexafluorophosphate (TBAP) to carry out the electrochemical exfoliation of bulk BP.[121] This process led to the formation of a few-layer phosphorene (FL-P) with a substantial area deprived of any surface functional

groups. To achieve this, BP crystals were utilized as the cathode, while a Pt sheet served as the anode. The application of voltage prompted the migration of tetrabutylammonium cations into the interlayer of bulk BP, resulting in an increase in volume, which indicated the separation of FL-P from bulk BP. Following this, 2D BP NSs were fabricated by using an electrochemical expansion technique through a variation of electrolytic solutions.[122–125] Ambrosi *et al.* (2017) also produced few-layer thick BP NSs from bulk BP crystals.[122] The team implemented an anodic potential to regulate the exfoliation efficiency as well as the fabrication of quality of BP NSs. Subsequently, Li *et al.* (2018) reported the ultrafast cathodic expansion of bulk BP using tetraalkylammonium salts as the electrolyte for producing highly crystalline FL BP flakes under ambient conditions.[123] In addition to this, Yang *et al.* (2018) fabricated BP NSs from bulk BP through electrochemical delamination and intercalation of cations like Li^+, Na^+, and tetra-alkyl-ammonium cations like tetra-methyl-ammonium (TMA^+) cations, tetra-ethyl-ammonium (TEA^+) cations, and tetra-*n*-butyl-ammonium (TBA^+) cations.[124] Moreover, interaction of bisulphate anions and TBA^+ stimulated the exfoliation towards yield up to 78%. Qiu *et al.* (2019) described cobaltous phytate functionalized BP NSs employing BP crystals as the cathode material and phytic acid as the electrolyte.[125] However, Xiao *et al.* (2018) developed a facile exfoliation approach to produce ultrathin BP NSs from bulk BP crystals.[126] The team utilized BP powder within a porous plastic tube with a cathode made of a Pt plate and an anode made of another Pt plate. Tetra-*n*-butyl ammonium hydrogen sulphate (–TBA·HSO_4) was applied using two electrodes soaked in a propylene carbonate solution and exposed to 30 V (12 hours). Additionally, after the electrochemical expansion, the expanded BP powder was submerged in pure propylene carbonate (PC) solution for 0.5 hours, filtered, followed by washing three times and dried in a vacuum oven (333 K, 8 hours) to produce BPNSs. The BP NSs in the schematic diagram ranged in size from 2 to 7 nm. Nevertheless, the oxygen content of the exfoliated BP NSs was lower than that of bulk BP, suggesting that the BP NSs may be partially recovered from oxidation or deterioration (Fig. 5e). Similarly, Wang *et al.* (2019) reported the fabrication of BP NSs by the delamination exfoliation technique employing TBA·HSO_4 solution.[127] Furthermore, Zu *et al.* (2019) successfully synthesized BP NSs at a gram scale within an hour utilizing the cathodic exfoliation approach.[128]

3.2.4 Chemical vapor deposition method. The primary purpose of the chemical vapor deposition (CVD) technology is to produce 2D materials. Using a two-step heating chemical vapor transfer process, Zhang *et al.* (2016) fabricated orthorhombic BP (*o*-BP) single crystals utilizing RP as a precursor and tin (Sn) and iodine (I_2) as mineralization additives (Fig. 5f).[129] The observed *o*-BP crystals have a narrow band gap of about 0.284 eV and yield of approximately 90%. The BP crystals appeared stable in an inert gas (such as Ar), and considerable thermal degradation wasn't seen until 330 °C. Furthermore, Smith *et al.* (2016) used an *in situ* CVD method to synthesize large-size BP NSs directly utilizing RP as the precursor.[130] However, this approach used a silicon substrate with a thin film coating around RP to reduce the challenges associated with encapsulating the ampoule. Even though the end products contain impurities and have many disadvantages compared to other processes, it is claimed to be inexpensive and adaptable for fabricating BP NSs.

3.2.5 Liquid-phase exfoliation method. This approach involves the dispersion of stacked bulk materials in solvents possessing adequate surface energy that resembles the bulk materials and subsequently utilizing ultrasonication to produce 2D NSs. Additionally, varying the exfoliation parameters, such as temperature, time, and centrifugal speed, may alter the thickness and size of 2D NSs. Many 2D NSs have been synthesized using this technique.[131–133] For the first time in 2014, Brent and team obtained a few layers of 2D NSs by the exfoliation of bulk BP using NMP (*N*-methyl-2-pyrrolidone) as a solvent.[38] The team observed that after 24 hours of exfoliation, the resulting BP NSs consisted of 3 to 5 layers of phosphorene (thickness varying between 3.5 and 5 nm and dimensions of about 200 × 200 nm). Nevertheless, after 48 hours, the observed BP NSs were composed of single and bilayer phosphorene with a thickness of 0.9–1.6 nm and a size of around 20 × 20 nm. Despite achieving the initial large-scale exfoliation of BP into 2D NSs, maintaining stability in common solvents like water posed a challenge, ultimately limiting its practical utility. Acknowledging the stability challenge, Guo *et al.* (2015) addressed the issue by synthesizing thin-layer phosphorene using a saturated NaOH–NMP solution.[134] Utilizing the basic NMP solvent the effective adsorption of hydroxide radicals on the surface of the phosphorene layer remarkably improved the stability of phosphorene in both NMP and water, which was validated by zeta potential results. Meanwhile, by modulating the speed of the centrifuge machine, the team obtained a uniform size and thickness of BP NSs. According to the AFM (Fig. 5g) and TEM (Fig. 5h) images, centrifugation at 12 000 rpm resulted in a diameter and thickness of about 670 nm and 5.3 ± 2.0 nm (5 to 12 layers), respectively. On the other hand, centrifugation (18 000 rpm) of the supernatant produced an average diameter and thickness of around 210 nm and 2.8 ± 1.5 nm, respectively, including 2 to 7 layers of phosphorene, as shown in Fig. 5 (i and j). Using this technique, Kang *et al.* (2015) fabricated BP NSs utilizing various solvents for sonication, such as isopropanol (IPA), DMF, acetone, ethanol, chloroform, hexane, and NMP.[135] They concluded that NMP was the best option out of all these solvents considered for synthesizing BP NSs. Subsequently, Yasaei *et al.* (2015) used this method to produce highly crystalline pure BP nanoflakes.[136] Compared to manually exfoliated BP nanoflakes, the exfoliated nanoflakes had significant electrical characteristics and were well-defended against degradation in the form of solution. Similarly, Lin *et al.* (2016) carried out ultrasonication utilizing ethanol, acetone,

NMP, and IPA and discovered that IPA produced the highest yield among all these solvents.[137] Furthermore, for the exfoliation of bulk BP, Zhang and collaborators (2016) used a range of solvents (different surface tensions), including NMP, DMF, dimethyl sulfoxide (DMSO), tetrahydrofuran (THF), IPA, ethanol, methanol, deionized water, and acetone.[138] Nevertheless, the team observed the correlation between the concentration of FL BP and surface tension for several solvents. Besides that, formamide exhibited an excellent yield of almost 38% of BP NSs, which was higher than that of widely used solvents like NMP, IPA, DMF, and so on. The resulting BP NSs demonstrated excellent crystallinity and tunable size distributions. Similarly, Jia *et al.* (2019) successfully isolated FL BP using NMP and titanium sulfonate ligand (TiL_4).[139] They observed that Ti (TiL_4) effectively utilizes the unshared electron pair of P (BP) by forming a coordinate bond between BP and TiL_4. As a result, TiL_4-modified BP exhibited remarkable resistance toward water and oxygen, which demonstrated exceptional stability of BP. Additionally, using this technique Zou and team (2018) performed photocatalytic H_2 production of about 1286 μmol h^{-1} g^{-1} by forming a 2D–2D BP/MoS_2 heterojunction.[85] Zhang and co-workers (2018) performed ultrasonication by sealing a conical bottle below 300 K for approximately 24 hours to obtain turbidity, followed by centrifugation at 3000 rpm for 20 min to remove residual BP.[140] Conversely, Yan and team (2018) produced evenly dispersed BP NSs by centrifugation at 6000 rpm for 20 min.[141] Moreover, Liu *et al.* (2018) isolated BP from the environment using organic solvents to a considerable extent.[142] However, BP tends to oxidise on exposure to air. Although organic solvents can prevent the BP NSs from oxidation, removing organic media is quite difficult. However, using the LPE method, a significant amount of BP NSs can be synthesized, producing considerable purity compared to other methods. From the above discussed exfoliation technique, bulk BP can be exfoliated by using organic solvents, which can prevent the oxidation of resulting NSs with a good amount of yield with an additional precaution towards the removal of organic media from the exfoliated NSs.

3.2.6 Pulsed laser technique. In this technology, a laser pulse has been used for the bombardment of the target and the deposition of bombardment plasma on the substrate for the growth of thin films. Researchers adopt this approach while producing thin films with a maximum of nanomaterials. Nevertheless, in 2015, Yang and colleagues used the pulsed laser deposition (PLD) approach to fabricate ultrathin BP films at about 150 °C. This was considered an advantage over the synthesis of bulk BP carried out at high pressure and high temperature.[143] The number of pulses impacted the thickness of the BP films, and hence, the thickness of BP films varied according to the number of pulses. Also, AFM was utilized to measure the film thickness, specifically shown in Fig. 5k. Moreover, field-effect transistors (FETs) were engaged for the first time to identify the p-type transistor characteristics in 2018 by Li *et al.*, which confirmed the hole as the charge carrier in fabricating BP ultrathin film.[144] According to RAMAN and IR spectroscopy, the produced BP thin film exhibited a crystal size range between 40 and 70 μm. However, the field-effect mobility of the BP thin-film was observed to be 160 cm^2 v^{-1} s^{-1} at RT along the armchair direction and reached up to 200 cm^2 v^{-1} s^{-1} around 90 K (Fig. 5l).

3.2.7 Solvothermal synthesis. In 2016, Zhang *et al.* developed BP NSs using ethanol as the solvent and RP as the precursor in a wet-chemical solvothermal method (Fig. 5m).[145] The team used commercial RP (0.5 g) and ethanol (50 mL). It was transferred inside a 200 mL reactor for about 24 hours while maintaining a temperature of around 400 °C and vessel pressure of around 50 bar, followed by sonication for half an hour using ethanol solution and centrifugation at about 10 000 rpm, and dried in a vacuum for 2 hours at 100 °C to produce the desired product, which appeared to have substantial electronic and optoelectronic applications. Furthermore, the AFM analysis demonstrated that the lateral size of BP NSs was about 1.0 μm along with a thickness of around 0.5–4 nm (Fig. 5n). After that, Tian and collaborators developed gram-scale FL BP NSs using a one-pot solvothermal method in 2018.[146] At first the team dissolved WP in ethylenediamine and noticed that WP temporarily changed into the RP intermediate during the process which indicated that the solution medium accelerated the transformation of RP into BP. They used a magnetic stirrer to prepare a solution of WP and ethylenediamine, which was then transferred to a 100 mL autoclave and heated for 12 hours at about 100 °C before cooling to RT to obtain a residue. This residue was then successively washed with benzene, ethanol, and distilled water before being dried overnight at 60 °C in a vacuum. During the process, precipitation was not observed below 60 °C; however, white crystals were formed above 140 °C instead of the expected BP NSs. Therefore, they confirmed that FL BP NSs with sizes ranging from 800–1000 nm were synthesized at reaction temperatures between 60 °C and 140 °C.

Reduction of energy consumption and efficiency in output is the main objective of research. Hence, in the future, CVD and PLD could be alternative approaches for synthesizing BP NSs, saving a significant amount of energy. Using these methods, BP NSs could be directly synthesized using RP as the precursor without the involvement of bulk BP. In addition, using these techniques, the accuracy and thickness of BP thin films can be well maintained compared to other methods. Using PLD, the adjustable thickness of BP NSs is achieved by adjusting the number of pulses. Therefore, these BP NSs can be used in making semiconductors and precision testing instruments. In addition, CVD can be utilized for commercial applications because it consumes less energy and synthesizes products having lower requirements, like catalysts and optical fiber. In addition, mechanical exfoliation techniques and electrochemical expansion approaches can't be excellent options for large-scale

production of BP NSs. Although LPE is commonly used to synthesize BP NSs, ultrasonic power and time-variation limit the output of BP NS synthesis. However, for the synthesis of BP NSs, researchers should improve methods like CVD and PLD to increase the yield and purity of BP NSs in the products.

3.3 Preparation of 0D black phosphorus quantum dots

Different dimensional oriented BP can be obtained by modulating various conditions and parameters during the preparation. In addition, because of edge effects and quantum confinement, 0D BP QDs have been the center of attraction for many researchers. Furthermore, the procedure for producing BP QDs resembled the methods used for synthesizing BP NSs. In 2015, using bulk BP crystals and ice-bath sonication, Zhang and colleagues, for the first time, successfully manufactured BP QDs.[147] In a mortar, the team added 5 mg of BP powder and 1 mL of NMP, and the mixture was thoroughly ground for about 20 minutes. The mixture was then placed into a glass vial and subjected to a 200 W power source and 3 hours of sonication in an ice bath. After centrifuging the mixture for about 20 minutes at 7000 rpm, BP QDs were found in the supernatant. The as-synthesized material exhibited thickness and lateral dimensions of around 1.9 and 4.9 nm, respectively. Moreover, the solution possessed remarkable stability in NMP. Sun *et al.* obtained BP QDs through liquid exfoliation in NMP, as shown in Fig. 6a, with lateral size and thickness of about 2.6 nm and 1.5 nm, respectively, using bath and probe sonication. A statistical investigation (100 QDs) was conducted to determine their adjacent sizes and heights using transmission electron microscopy (TEM) and atomic force microscopy (AFM), and the results are illustrated in Fig. 6b and c, respectively.[148] Similarly, Gao *et al.* (2016) successfully fabricated extremely thin layer QDs having

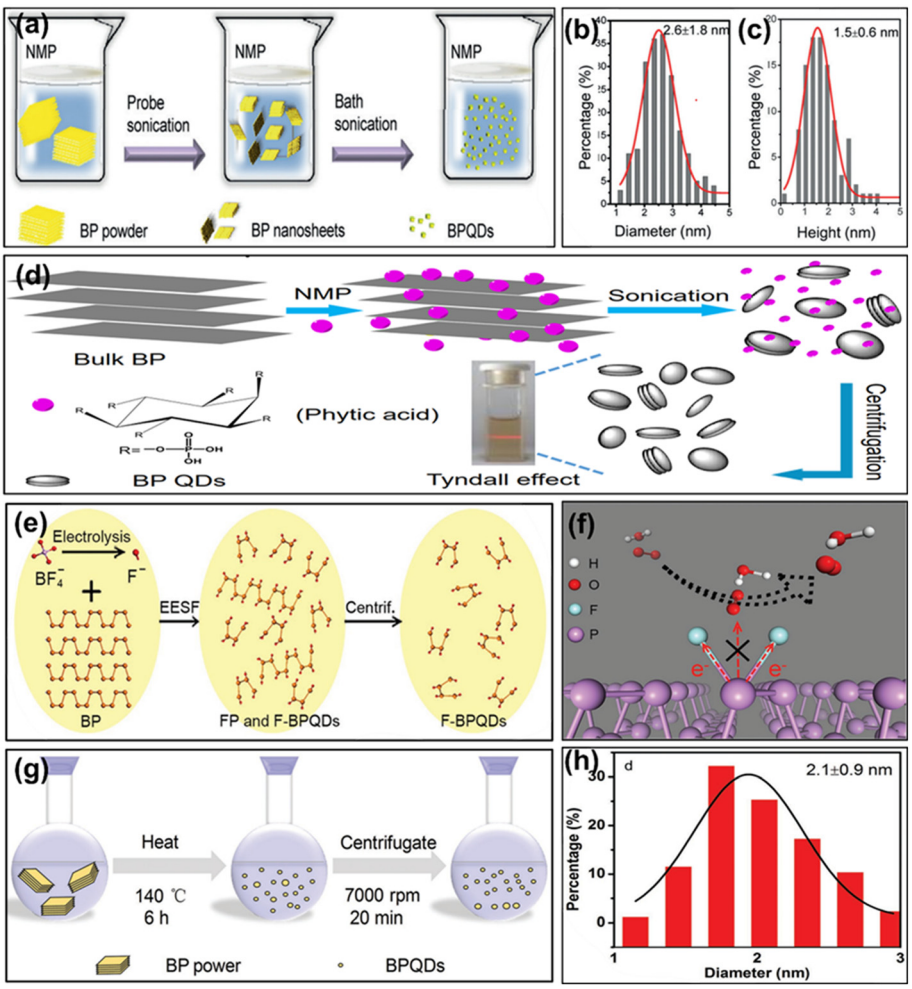

Fig. 6 (a) The fabrication method of BP QDs. (b and c) The measurement of the lateral dimensions and heights (100 BP QDs) was conducted through TEM and AFM, respectively. Adapted with permission.[148] Copyright 2018, Wiley; (d) bulk BP exfoliation into BP QDs in the presence of phytic acid. Adapted with permission.[149] Copyright 2016, Royal Society of Chemistry; (e) fabrication of F-BP QDs; (f) scheme demonstrating how F-BP QDs maintain stability when exposed to the atmosphere. Adapted with permission.[151] Copyright 2018, Wiley; (g) the production of BP QDs *via* a solvothermal approach; (h) the measurement of the lateral dimensions (100 BP QDs) conducted through TEM. Adapted with permission.[153] Copyright 2016, Wiley.

consistent size (3.4 nm) using phytic acid *via* the LPE technique, as depicted in Fig. 6d.[149] Moreover, the interaction between phytic acid and BP (rich in phosphorus and hydroxyl groups) exfoliated the bulk BP into QDs. Subsequently, Chen *et al.* (2017) also fabricated BP QDs, with an average size of about 5.2 nm, employing ultrasonication and centrifugation while using IPA as the solvent.[150] Furthermore, they noticed that at RT, BP QDs exhibited good dispersibility and stability in IPA, although a significant amount of aggregation was seen when stored for a month. However, in 2018, Tang and colleagues introduced a simple electrochemical exfoliation method (Fig. 6e) to produce highly specific fluorinated BP QDs, as depicted in Fig. 6f. These QDs had an average dimension of approximately 5 nm in size and a thickness of about 2 nm.[151] Adding more, Zhu *et al.* (2016) fabricated BP QDs from bulk BP crystals using a standard kitchen mixer by a top-down synthetic approach.[152] The remarkable crystallinity of the BP QDs led to the

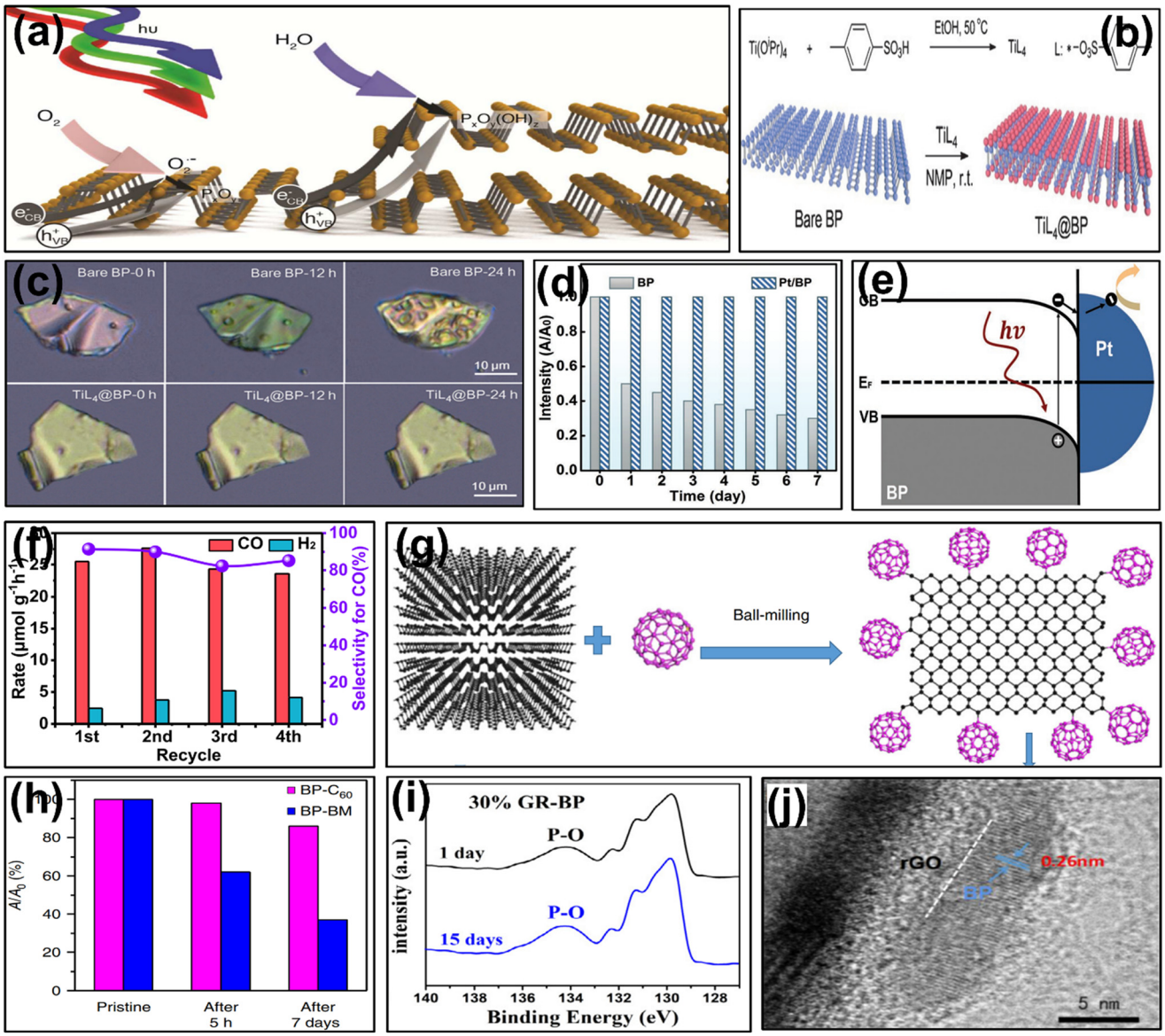

Fig. 7 (a) A graphical illustration of the mechanism for oxidative degradation of BP. Adapted with permission.[161] Copyright 2017, American Chemical Society; (b) synthesis approach for the formation of TiL_4 and formation of TiL_4@BP over the surface of BP, and (c) optical images demonstrating the stability of bare BP and TiL_4@BP NSs under air exposure for 24 hours. Adapted with permission.[165] Copyright 2016, Wiley; (d) stability mechanism depicting the vis-light absorption for BP along with the Pt/BP catalyst when stored in water, and (e) schematic illustration of the band structure and ET mechanism at the Pt/BP interface. Adapted with permission.[167] Copyright 2018, Wiley; (f) photocatalytic recycling experiments towards CO_2 reduction for stability of Co_2P/BP. Adapted with permission.[171] Copyright 2017, American Chemical Society; (g) schematic representation of the synthesis of BP–C_{60}, and (h) variation ratios of absorption of the dispersed BP–C_{60} hybrid and BP–BM heterostructure in water in different time intervals. Adapted with permission.[178] Copyright 2018, Nature; (i) XPS analysis corresponding to P (2p) peaks of the GR–BP heterostructure. Adapted with permission.[179] Copyright 2019, Elsevier. (j) TEM analysis of the rGO@BP@rGO heterostructure. Adapted with permission.[180] Copyright 2019, American Chemical Society.

synthesis of additional layered 2D materials (LTMs) for commercialization. Furthermore, the solvothermal approach is an alternate method for producing BP QDs on a big scale. In 2016, Xu and colleagues employed the solvothermal method to produce ultrasmall BP QDs from bulk BP, as illustrated in Fig. 6g, with an average size of approximately 2.1 nm (Fig. 6h).[153] They initiated the process by grinding BP crystals into a powder, subsequently dispersing the powder in a saturated NaOH/NMP solution, and continuously stirring it for approximately 6 hours at 413 K. After centrifugation and separation of the resulting suspension, the BP QDs were obtained. Subsequently, Gu and his colleagues employed a solvothermal method to fabricate BP QDs with an approximate size of 1.76 nm.[154] Following the previous steps, they first dispersed bulk BP in NMP and then vigorously stirred it for approximately 12 hours at 413 K in a nitrogen environment to produce the BP QDs.

The choice of synthesis method can influence the specific surface area, defect density, and other properties that impact the photocatalytic performance of BP. The unique electronic structure of BP, along with its tunable bandgap, makes it a potential catalyst for various photocatalytic reactions. Synthesis of bulk BP mainly focused on applying high-temperature and high-pressure methods which is not appreciable in laboratory uses. Therefore, based on fabrication methods for graphene, 2D BP NSs have been explored for various photocatalytic reactions and HER.[155,156] The newly developed BP NSs photocatalyst can be used frequently for various photocatalytic activities. Presently, PLD and CVD techniques are widely utilized to synthesize BP NSs. Additionally, by expanding the lateral dimensions of BP NSs, more active sites can be developed for improving the photocatalytic activity of BP. Hence, 0D BP QDs have been synthesized following the synthetic procedure of 2D BP NSs. As a result, owing to the large number of active sites at the edges, BP QDs are considered especially for the photocatalytic HER.[157,158] Although varying conditions and features may produce different dimensions of BP materials, it is essential to note that the synthesis of BP can be challenging due to its reactivity and sensitivity to oxygen and moisture. Therefore, scientists take appropriate precautions to ensure that the synthesis is conducted in an inert or controlled atmosphere to prevent oxidation or degradation of the BP material.

4. Factors underlying modifications and stability of BP

In the domain of photocatalysis, the inherent instability of pristine BP catalysts poses a challenge as they are prone to oxidation when exposed to air (O_2), light, and water. This susceptibility arises from the chemical activity of lone pair electrons of P-atoms (BP), which readily interact with oxygen (O_2) molecules.[159,160] In this context, the general mechanism of deterioration of BP due to oxidative processes is concisely outlined in Fig. 7a.[161] It was observed that under light exposure, O_2 molecules react with photoexcited electrons on the surface of BP, generating superoxide radicals ($^{\bullet}O_2^-$) which leads to the formation of oxidized P, *i.e.*, P_xO_y, and subsequently P_xO_y transforms into phosphates and phosphate ions in the presence of water. Furthermore, as the degradation depends upon layers, the rate of oxidative degradation increases with a lower number of BP layers ultimately reducing the stability and photocatalytic activity of BP. To address this issue, various strategies have been explored to prevent oxidative degradation that ultimately improves the stability and significantly enhances the overall photocatalytic performance of BP-based systems.

An approach involves physically enhancing the stability of BP by reducing its surface exposure and forming a shielding layer on its surface by using a suitable and resilient material. Additionally, the degradation of BP can be prevented by isolating ambient oxygen and water, achieved by introducing specific ions or molecules onto the BP surface that recombine with the active lone pair of electrons on BP.[162] To address the degradation of BP under ambient environmental conditions, Ryder *et al.* in 2016, proposed a functionalization approach for the modification of FL BP using aryl diazonium salts.[163] The team observed that the functionalization of exfoliated BP effectively mitigates the chemical degradation for three weeks on exposure to ambient conditions. Furthermore, the functionalization of passivated BP flakes maintained a stable morphology even after 10 days of prolonged exposure that was detected *via* AFM analysis, which implies that the development of covalent bonding between the phosphorus atom and aryl group, *i.e.*, the formation of a P–C covalent bond, successfully prevented BP from interacting with ambient oxygen and water. However, excessive functionalization leads to the loss of XPS peaks, Raman modes, and conductivity of BP. Further, Hirsch and team (2016) presented a wet-chemical approach for the functionalization of bulk BP involving polycyclic aromatic compounds like perylene bisimide and 7,7,8,8-tetracyano-*p*-quinoidimethane (TCNQ).[164] The group explored the existence of noncovalent bonding between BP and these aromatic compounds using both experimental methods and computational calculations that facilitated the exfoliation of bulk BP into FL BP. TCNQ prompted ET from BP to the organic component, and DFT calculations supported the stabilization of a positive charge on the BP surface by underlying layers. Introducing perylene diimide notably boosted resistance against oxygen-induced degradation. The efficacy of this approach in enhancing the stability of BP NSs was confirmed through theoretical calculations and various experimental techniques, including Raman spectroscopy, TEM, and AFM analysis. Similarly, Zhao *et al.* (2016) successfully explored the stability of the titanium sulfonate ligand (TiL_4) and BP@TiL_4 heterostructure as shown in Fig. 7b.[165] The team noticed that the formation of a coordinate bond between P (BP) and Ti (TiL_4) that effectively utilizes lone pair electrons of P, which significantly enhanced the stability of FL BP over an extended period when the

compound was allowed to be exposed to air and disperse in water under ambient conditions (Fig. 7c). This stability is attributed to the P–Ti coordination thoroughly investigated using photothermal analysis, XPS analysis, optical images, Raman, and absorption spectra, which consistently indicated that BP@TiL_4 NSs maintain excellent stability.

Besides, to increase the stability and photocatalytic efficacy of BP, metal nanoparticles have been recently explored.[166–168] Bai and group deposited ultrathin Pt nanoparticles over BP NSs to produce stable 2D Pt/BP nanocomposites.[167] This modification demonstrated strong Pt–P interactions analysed *via* DFT calculations and XPS characterization. Furthermore, the formation of a surface Pt–P_xO_y complex effectively shields the BP NSs from oxidative decomposition, ensuring their outstanding durability. The Pt/BP materials also demonstrated notable resilience during a 7 day immersion in water (Fig. 7d), with no noticeable degradation for at least 15 days under typical ambient conditions, in contrast to the pristine BP NSs. Additionally, at the surface of the BP/Pt interface, the team noticed the development of a Schottky barrier that facilitated the transfer of photoexcited electrons from BP to the BP/Pt interface (Fig. 7e). Additionally, the Pt/BP materials recovered after each cycle experienced no notable alterations in morphology during their successful recycling and reuse for a minimum of 5 repetitions.

Furthermore, several researchers have found that growing metal phosphides directly on the BP surface, like Ni_2P,[169] CoP,[46] and Co_2P,[170–172] can enhance the stability of BP under ambient conditions. These metal phosphides also act as effective cocatalysts, boosting the photocatalytic efficiency of BP. Zhu and co-workers recently developed a method to synthesize Co_2P nanoparticles on the BP surface.[171] Using this strategy the developed Co_2P/BP photocatalysts exhibited less oxidative erosion to Co_2P/BP compared to pristine BP when exposed to oxygen over time, as evident from XPS spectra. Hence, the team confirmed that loading Co_2P over the surface of the BP effectively reduced the O_2 exposure, subsequently enhancing the stability of the material. Moreover, extended visible light exposure showed that Co_2P/BP catalysts maintained excellent performance, demonstrated in photocatalytic cycling experiments as shown in Fig. 7f. Adding more, Co_2P/BP exhibited around 1.5 times higher photocatalytic CO_2 reduction activity compared to pure BP. This improvement was likely to be restricted by the close interface between BP and Co_2P, facilitating ET from BP to the Co_2P cocatalyst and subsequently, CO_2 molecules adsorbed on the Co_2P surface.

Subsequently, fullerenes such as C_{60} are categorized within the nanocarbon family due to their high electron absorption tendency, hydrophobicity, and aromatic behaviour, showcasing remarkable resilience in the presence of air, light, and water.[173,174] These characteristics have potential uses in the fields of bioscience and catalysis.[175–177] Subsequently, Zhu *et al.* employed an eco-friendly ball milling method to selectively form covalent bonds between C_{60} and the edges of 2D BP NSs, as depicted in Fig. 7g.[178] The team made a comparison between the BP@C_{60} hybrid and BP@BM heterostructure (BP with LiOH as an additive, termed as BM) by dispersing both hybrids in water for a week under normal atmospheric conditions. They observed that BP@C_{60} maintained an absorbance of about 86%, notably higher than the dispersion of BP–BM, as depicted in Fig. 7h. Furthermore, the BP@C_{60}hybrid displayed additional stability owing to the strong P–C covalent bonding interactions that bound the hydrophobic C_{60} molecules, which effectively shielded BP NSs from degradation caused by air, water, and light. Additionally, this bonding interaction triggered the transfer of photoexcited electrons from BP to C_{60}, thereby delaying the reduction of charge recombination rate and enhancing photocatalytic activity. Recently, graphene (GR) was introduced to enhance the photocatalytic activity as well as to increase the stability of BP by designing appropriate heterostructures. For instance, Zhang *et al.* fabricated a GR–BP photocatalyst using the one-pot CVT method, resulting in enhanced stability of BP due to the formation of P–C bonds during synthesis.[179] It was noticed that under air exposure the intensity of the P–O peak increased remarkably in the GR–BP heterostructure (Fig. 7i). This finding validated the outstanding stability of the BP nanomaterial. Additionally, the inclusion of GR facilitated better separation of charge carriers, leading to outstanding photocatalytic performance in degrading 2-chlorophenol. In another work, Ge *et al.* (2020) developed a stable metal-free heterostructure comprising reduced graphene oxide (rGO) encapsulating BP by aggregating GO NSs and BP in an aqueous solution, followed by lyophilization and partial reduction.[180] During lyophilization, the surface of rGO NSs was modified by enveloping the BP NSs from all sides, forming a sandwich-like structure termed rGO@BP@rGO. As depicted in Fig. 7j, a thick coating of disorganized GO enveloped the surface of individual exfoliated BP NSs, providing effective shielding

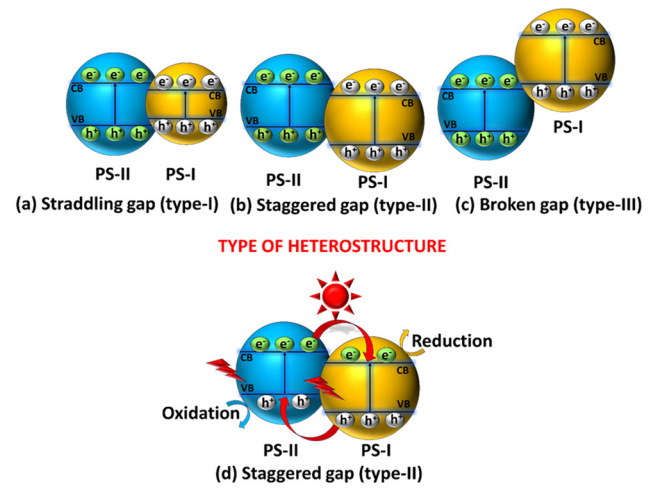

Scheme 2 Schematic illustration of the types of heterostructures: (a) type-I, (b) type-II, (c) type-III, and (d) DCT mechanism.

against direct air exposure and notably enhancing the stability of BP and also facilitating the effective transfer and segregation of photoinduced charge carriers resulting in increment of catalytic performance.

5. Charge carrier transfer mechanisms in photocatalysis

In the case of composite materials, the VB and CB arrangement leads to the formation of various types of heterojunctions in photocatalysis. These heterojunctions include type-I (straddled), type-II (staggered), and type-III (broken), and they play crucial roles in facilitating the movement of charge carriers. In a straddling band alignment, one semiconductor (PS-I) with a narrower band gap is enclosed by band edges (VB and CB) of another semiconductor (PS-II) having a wider band gap, as depicted in Scheme 2a. In addition, the most commonly used CT mechanism, known as the type-II heterojunction, has the band edge alignment of PS-II above the corresponding band edges of PS-I, as demonstrated in Scheme 2b. In the case of the broken type (Scheme 2c), the energy bands/band edges of the two semiconductors do not overlap; more specifically, the band gap of PS-I is located above the CB of PS-II. Among those listed above, the type-II heterostructure, which significantly enhances the spatial separation of carriers, known as DCT, is the most desired heterojunction and is commonly observed in photocatalysis (Scheme 2d). These findings led to a decrease in the recombination rate, extending the lifespan of relevant charge carriers and enabling redox processes in various semiconductors.[181] However, the staggered type mechanism has multiple drawbacks that hinder its extensive utilization in applications related to AP. For instance, the movement of electrons from the CB of PS-II to the CB of PS-I and the migration of holes from the VB of PS-I to the VB of PS-II are quite challenging due to electrostatic forces of repulsion that arise because of the interaction of like charges. As holes gather at the VB with a lower oxidation potential and electrons at the CB with a lower reduction potential, it ultimately weakens the overall redox ability of the system. Consequently, achieving a higher redox potential system is still a challenging task that requires an alternative heterostructure. Therefore, in contrast to the DCT mode, Z-scheme type heterojunction systems have received significant attention to address this issue.

6. Z-scheme photocatalysis

To maximize the redox potential of heterostructure-based photocatalysts, Bard *et al.* (1979) introduced artificial photocatalytic systems that use a concept called Z-scheme.[182] This approach involves two distinct photocatalysts, one excels in oxidation and another in reduction. The photocatalyst with a lower VB potential (PS-I) exhibits a remarkable oxidation tendency, whereas the higher CB potential photocatalyst (PS-II) demonstrates excellent reduction abilities. Similar to the naturally occurring Z-scheme, photo-excited electrons (e^-) from the CB of PS-I move towards the VB of PS-II. Subsequently, the holes (h^+) that remain in the VB (PS-I) exhibit robust oxidation, and the photo-produced electrons (e^-) display potent reduction. Therefore, based on the presence or absence of a mediator to facilitate the CT mechanism, the Z-scheme heterostructures are classified into three categories as depicted in Scheme 3.

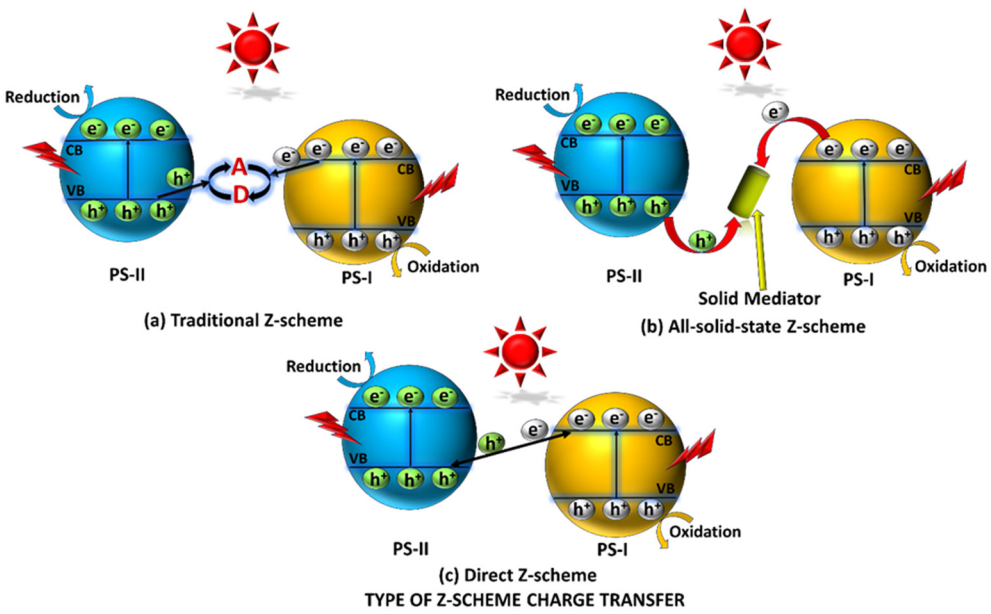

Scheme 3 Representation of various Z-scheme CT mechanisms: (a) the conventional Z-scheme; (b) all-solid-state Z-scheme; (c) direct Z-scheme.

6.1 Conventional Z-scheme photocatalysts

Traditional Z-scheme based systems belong to a family of substances employed in photocatalysis, a method that uses light energy to drive chemical reactions. The Z-scheme refers to a specific mechanism of ET between two different semiconductors to enhance the efficiency of photocatalysis. In the case of a typical Z-scheme type photocatalytic system, PS-I and PS-II are integrated through an appropriate acceptor (A) and (D) donor unit, which acts as an ion mediator or redox shuttle to develop the Z-scheme framework. Most importantly, these two semiconductors are not in direct physical contact (Scheme 3a). Upon exposure to solar radiation, the photoinduced electrons moved from the CB (PS-I) to the VB (PS-II) *via* a mediator pair, demonstrated below.

$$\text{(A)Acceptor} + \text{electron } (e^-) \text{ from CB(PS-I)} = \text{(D)donor}$$

$$\text{(D)Donor} + \text{hole } (h^+) \text{ from VB(PS-II)} = \text{(A)acceptor}$$

In the photocatalytic reaction, A is reduced to D by capturing electrons from the CB (PS-I). Subsequently, D is oxidised into A by the interaction of photoproduced holes from the VB (PS-II). Because of this, photoexcited electrons migrate from the CB (PS-I) to the VB (PS-II), which resembles the Z-scheme system. The holes in the VB of PS-I and the electron density in the CB of PS-II result in spatial carrier separation that decreases the recombination pace. The concentration of charge carriers at various energy levels promotes surface reduction and oxidation reactions to magnify the redox processes. The conventional Z-scheme heterojunction has outstanding photocatalytic properties but has certain downsides, *i.e.*, the possibility of mediator-induced back-reaction in which the photoexcited electrons of the CB (PS-I) may interact with holes of the VB (PS-II) through the mediator (as discussed above) reducing the actual number of photoexcited charge carriers and ultimately decreasing the overall redox capacity. These are few reported shuttle redox ion couples Fe(II)/Fe(III),[183,184] $[Co(bpy)_3]^{3+/2+}$,[185] $[Co(phen)_3]^{3+/2+}$,[186] I^{3-}/I^-,[187] and I^-/IO^{3-}.[188]

In a nutshell, conventional Z-scheme photocatalysts are effective but face several challenges related to potential back-reactions, which impact their overall performance.

6.2 All-solid-state Z-scheme photocatalysts

Conventional photocatalysts often utilize liquid or powder-based systems, which have limitations such as poor stability, difficulties in separating reactants and products, and limited application in specific environmental conditions. Solid photocatalysts aim to address these challenges using solid materials as Z-scheme type components. It is an updated or 2nd-generation Z-scheme based photocatalyst that replaces the former redox pair concept of a conventional Z-scheme oriented photocatalyst with a solid electronic conductor, allowing the movements of charge carriers between the combining materials (Scheme 3b).[189–191] The all-solid-state Z-scheme photocatalysis concept was first introduced by Tada and team using 'Au' as the electron mediator between two semiconductors.[192] Additionally, noble metals like Ag, Au, or Cu, as well as carbon-based materials such as graphene, graphene oxide (GO), reduced graphene oxide (RGO), carbon dots (CDs), and carbon nanotubes (CNTs) may be used as solid-state electron mediators.[193,194] Moreover, by the introduction of a solid channelizer at the junction of two semiconductors, the development of an ohmic contact takes place that successfully reduces the contact resistance.[195] This, in turn, decreased the path for migration of electrons between two semiconductors due to the ohmic contact, preventing the possibility of the previously mentioned back-reaction arising out of redox mediator couples. Moreover, the previously described reverse reactions that resulted from a mediator redox couple can be entirely prevented by conserving highly oxidative holes that are present in the VB (PS-I) and more reductive electrons at the CB (PS-II), successfully accelerating the forward reaction. In this case, all-solid-state Z-scheme systems are versatile and can be utilized in both liquid and gaseous conditions, broadening their range of applications. Furthermore, noble metals are expensive, possess photo-corrosive properties, and have shielding effects. Therefore, there is a need for further research and development to address these limitations before widespread commercialization.

6.3 Direct Z-scheme photocatalysts

Recently, Z-scheme based nanocomposite systems, as illustrated in Scheme 3c, have been referred to as direct Z-scheme photocatalysis because they don't rely on a mediator to attach the semiconductors. Instead, they come into direct surface contact.[196,197] Wang *et al.* (2009), for the first time, introduced a mediator-free direct Z-scheme nanocomposite, which completely eradicated the drawbacks (back-reactions, photo-corrosion, light-shielding effects) associated with the above two discussed Z-scheme types and thus gained more interest in the field of AP.[198] Furthermore, the difference in Fermi energy levels facilitates the operation of two semiconductors. This leads to a redistribution of charge, as demonstrated in Scheme 4a. Consequently, the movement of electrons from a higher Fermi level (PS-II) to a lower Fermi level (PS-I) generates an IEF. This electric field, in turn, induces an interfacial band bending by forming a potential barrier. In addition, the IEF plays a vital role in the determination of the migration of charge carriers (Scheme 4b). The directional alignment of band structures in the Z-scheme pattern corresponds to a type-II heterostructure, as illustrated in Scheme 4c. In this arrangement, the electrons that are highly reducing present in the CB (PS-I) and the holes having strong oxidising nature present in the VB (PS-II) lag behind the relatively low energetic electrons and holes present in the CB (PS-II) and

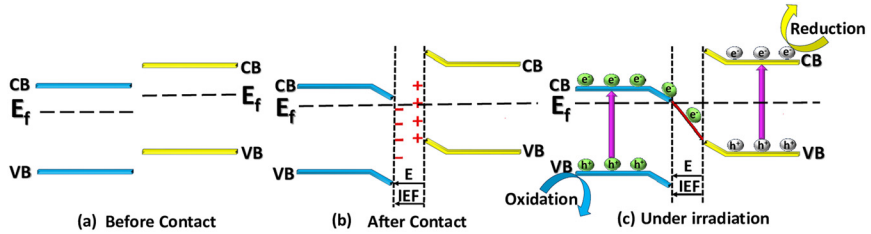

Scheme 4 Schematic representation of the direct Z-scheme (formation of band alignment and band bending): (a) before, (b) after, and (c) under light irradiation.

VB (PS-I) respectively. Therefore, the electrons in the CB (PS-I) and the holes in the VB (PS-II) take part in the redox reactions over the surface of the photocatalyst. Hence, the chances of recombination of bulk charge carriers are reduced due to the absence of electron carriers. In addition, since no noble or precious metals are used as electron mediators, the construction of a direct Z-scheme composite is economically viable, which minimizes the effect of light shielding. Therefore, Z-scheme oriented systems have attracted great interest in various photocatalytic applications. The efficient separation of charge carriers and the potential utilization of a wider spectrum of solar radiation make these systems attractive for sustainable energy conversion processes and environmental regeneration. Consequently, direct Z-scheme systems have become a focal point of interest in various applications in photocatalysis.

6.4 Advantages and disadvantages of Z-scheme systems

As mentioned above, Z-scheme based heterostructures exhibit higher efficacy towards segregation of e^-–h^+ pairs that demonstrate robust redox ability for photocatalytic responses towards a broad spectrum of solar light absorption. Subsequently, these heterostructures absorb light across a wide range of wavelengths, enhancing the overall photocatalytic performance. Furthermore, the efficient utilization of the solar spectrum enables Z-scheme heterostructures to exhibit various applications for renewable energy production and multi-step reactions like photocatalytic conversion of CO_2, degradation of pollutants, and photocatalytic splitting of water, addressing various energy and environmental challenges.

However, despite these promising attributes, the development is still in its early stages and requires further attention. The realization of the full potential of Z-scheme heterostructures faces multiple challenges due to the inefficient movement of charge carriers. Additionally, maintaining optimal utilization of the interface contact between oxidised and reduced components proves challenging due to the sensitivity of Z-scheme heterostructures at the semiconductor interfaces. To achieve optimal photocatalytic responses, it is imperative to use suitable photocatalysts that match the desired redox potential for constructing Z-scheme heterostructures. Furthermore, introducing advanced characterization techniques is necessary for a comprehensive understanding of electronic transport mechanisms. Therefore, while Z-scheme heterostructures offer several advantages in terms of efficient charge separation and broad light absorption, addressing the challenges related to limited efficiency and complex interfaces is crucial for their practical applications. Addressing these challenges through ongoing research and development efforts is essential to overcome these limitations and unlocks the full potential of Z-scheme heterostructures for various photocatalytic applications. In addition, the year-wise progress of Z-schemes and advancements in Z-scheme based BP heterojunctions towards photocatalytic H_2 generation is depicted in the Scheme 5.

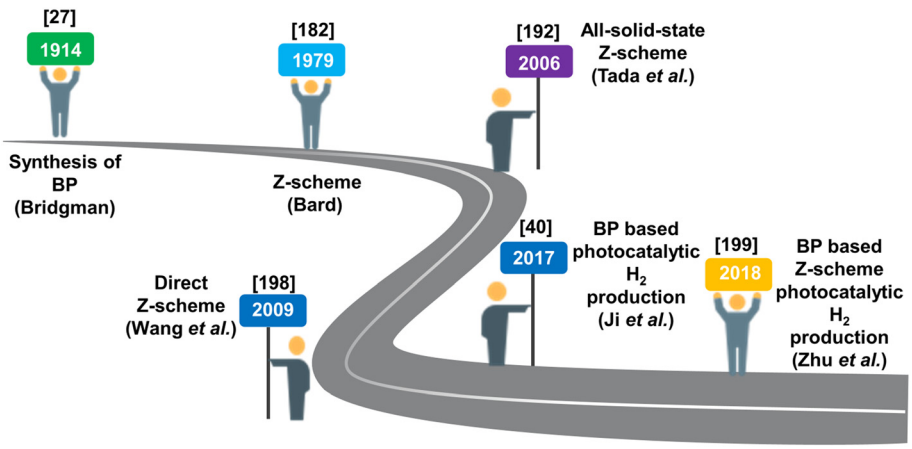

Scheme 5 Progress in the Z-scheme heterojunction and photocatalytic H_2 generation, highlighting the contributions of authors.

7. Z-scheme based black phosphorus systems for photocatalytic H_2 evolution

Semiconductor-driven photocatalytic H_2 evolution from water is the most promising, economically viable, and environmentally benign strategy to address the growing demands for sustainable fossil fuel alternatives. In this regard, extensive research has been done, but the benchmark efficiency has not yet been achieved to industrialise the process. Among many, Z-scheme charge dynamic oriented BP-based photocatalysts showed excellent response, which made researchers explore and get involved more in this kind of system. Therefore, the current review discussed several recently reported articles (narrated below), findings, and observations in brief to communicate the development and advancement made so far in this context. Further, Table 1 depicts the detailed experimental conditions of the included articles for better understanding.

7.1 BP/$BiVO_4$ heterostructure

For the first time, in 2018, a 2D heterostructure was constructed using BP and $BiVO_4$ that simultaneously split water into H_2 and O_2 without sacrificial chemical agents and external biasing. In this context, Zhu *et al.* fabricated a series of BP/$BiVO_4$ nanocomposites (varying BP wt%) *via* a sono chemical assisted self-assemble method where BP acts as the reduction site and $BiVO_4$ as the oxidation centre.[199] The optimum catalyst, *i.e.*, 20 wt% BP/$BiVO_4$, displays the best activity with an H_2 evolution rate of 160 μmol g^{-1} h^{-1} (Fig. 8a) and AQY of 0.89% ($\lambda > 420$ nm) under visible light without any sacrificial agent and outside potential. The binary hybrid shows excellent stability for 9 hours with negligible change in generation velocity, as shown in Fig. 8b. The enhanced activity corresponds to effective exciton separation by the Z-scheme CT route (Fig. 8c), as confirmed through EIS and photocurrent measurements. The team also explored the variation in H_2 evolution rate in the presence of a co-catalyst, sacrificial agent, and change in photon flux. The heterostructure formation between the semiconductors is well evidenced by HRTEM images and the origin of the heterojunction at the interfacial region *via* a shift in the binding energy of constituting elements of the composite from the XPS spectra. Further, the MS measurement results give a brief idea about the band alignment of BP and $BiVO_4$ in the composite, which favours the Z-scheme type CT pathway leading to the availability of highly oxidising holes ($BiVO_4$) and highly reducing electrons (BP) at respective sites. Moreover, the proposed Z-scheme mechanism is well validated by discussing the change in carrier lifetime of the composite compared to neat materials as observed through femtosecond time-resolved diffuse reflectance (femtosecond TDR) spectroscopy. This work demonstrates the promising future for overall water splitting using BP-based Z-scheme type heterostructure charge migration.

7.2 BP/monolayer Bi_2WO_6 heterostructure

Splitting pure H_2O to produce H_2 using only a bare BP photocatalyst poses a challenging task due to rapid interfacial charge recombination and a high rate of decomposition, which hinders H_2 production over the surface of BP NSs. To overcome these limitations, Hu and co-workers devised an effective approach by designing a promising 2D/2D BP/monolayer Bi_2WO_6 (MBWO) Z-scheme heterostructure by following a multistep process.[200] This design reduces the photogenerated e^-–h^+ recombination and suppresses the decomposition rate, leading to promising results. The team carried out a HER experiment for various BP/MBWO heterostructures with different BP contents utilizing $H_2PtCl_6{\cdot}6H_2O$ as a co-catalyst. The 12% BP/MBWO heterostructure exhibited the optimum H_2 generation rate, about 21 042 μmol g^{-1} (300 W Xe lamp). The outcome was

Table 1 Representation of the discussed BP-based Z-scheme heterojunction for photocatalytic H_2 evolution

SL. No	Photocatalyst	Lamp used	Experimental conditions	Ref.	Year
7.1	BP/$BiVO_4$	Xe lamp (320 W, intensity – 400 mW cm^{-2}, $\lambda_{cutoff\ filter} > 420$ nm)	5 mg sample added in 8 mL H_2O solution	199	2018
7.2	BP/monolayer Bi_2WO_6	Xe light (300 W)	20 mg sample (co-catalyst: 3 wt% Pt) added in 90 mL deionised and 10 mL TEOA (sacrificial agent)	200	2019
7.3	BP/RP	White LED lamp (20 × 10 W, $\lambda_{cutoff\ filter} > 420$ nm)	2 mg photocatalyst added in 6 mL water	201	2019
7.4	BP/RP-QD	LED lamp (12 W, $\lambda = 420 \pm 10$ nm)	1 mg photocatalyst (co-catalyst: 2 wt% Co) added to 5 mL water	202	2019
7.5	NYF/Ag_3PO_4/BP	Laser light (10 W, $\lambda = 980$ nm)	15 mg sample added in 100 mL of a glycerol–H_2O mixture (50 vol% glycerol)	203	2019
7.6	BP/WN	Xe lamp (320 W, $\lambda_{cutoff\ filter} > 420/700$ nm)	10 mg photocatalyst added in 10 mL of deionized water	204	2020
7.7	$ZnFe_2O_4$/BP	Xe lamp (300 W, $\lambda_{cutoff\ filter} > 420$ nm and 820 nm)	20 mg catalyst added in 10 mL methanol and 50 mL H_2O	205	2021
7.8	BP/Fe_2O_3	Xe lamp (300 W, $\lambda > 420$ nm)	10 mg sample (co-catalyst: 3 wt% Pt) added in 50 mL deionised water; and 10 vol% TEOA as sacrificial agent	206	2021
7.9	BP/MoO_{3-x}	Xe lamp (320 W, cut-off type AM1.5 or 700 nm)	10 mg photocatalyst added in 10 mL of deionized water	207	2022

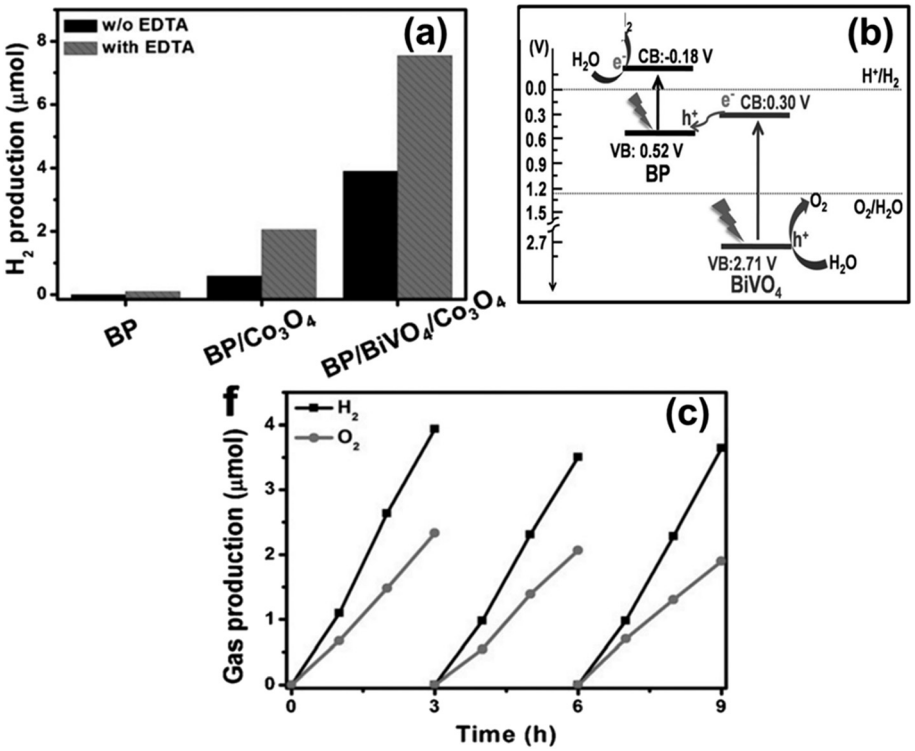

Fig. 8 (a) Comparison plot of solar H_2 evolution using various catalysts, (b) an assessment of the long-term stability of BP/$BiVO_4$/Co_3O_4 in the context of photocatalytic water splitting, and (c) Z-scheme mechanism illustrating overall water splitting facilitated by BP/$BiVO_4$. Adapted with permission.[199] Copyright 2018, Wiley.

remarkably 2.6 times and 9.15 times higher than pure MBWO and pristine MBWO, respectively (Fig. 9a). Additionally, the team analysed the photocatalytic efficiency for H_2 production for five cycles (25 hours), which was enhanced by using TEOA as a sacrificial agent just after the third cycle, as depicted in Fig. 9b. To understand the underlying mechanism, the team proposed a Z-scheme photocatalytic process (Fig. 9c), which was well confirmed by monitoring of the active $^{\bullet}O_2^-$, $^{\bullet}OH$, NO_2, and NO^{3-} species tracing experiment through EPR analysis over the surface of BP NSs with MBWO. This interaction between the two semiconductors was confirmed *via* SEM, TEM, and HRTEM studies, revealing an intimate interface between them. In conclusion, the study highlighted the numerous advantages of 2D/2D BP nanosheet-based heterostructures, which open up new possibilities in the field of photocatalysis for the treatment of environmental pollution and renewable energy applications.

7.3 BP/RP binary heterostructure

In another work, Liu and co-workers in 2019 successfully designed a direct Z-scheme orientated BP/RP heterojunction *via* an *in situ* wet-chemistry method for photocatalytic pure water splitting to produce H_2 without any sacrificial agents.[201] The designed heterostructure exhibited an excellent H_2 production rate of about 0.33 mmol g^{-1} h^{-1}, which was 3.3 and 2.5 times higher than RP and the mixture of BP and RP, respectively (Fig. 10a). Among various non-noble metal co-catalysts like Fe, Co, Ni, and Cu, the optimum H_2 evolution activity was observed for 1.4 wt% Co of about 2.96 mmol g^{-1} h^{-1} (20 × 10 W, $\lambda > 420$ nm) with an apparent quantum efficiency (AQE) of 1.21% at 420 nm (Fig. 10b). The heterostructure displayed excellent stability for 4 consecutive runs (240 minutes) as shown in Fig. 10c. The observed improvement in activity corresponds to effective carrier separation and transfer efficiency realized *via* Z-scheme charge dynamics shown in Fig. 10d. Additionally, Co incorporation expressed the final retention of 82% photocatalytic activity compared to the initial activity after four cycles (12 hours). The synthesized BP/RP heterostructure was well analysed using TEM and AFM. Furthermore, the Z-scheme mechanism was confirmed by observing time-resolved transient absorption spectra (TAS) (excited at 400 nm). Moreover, the photoelectrochemical (PEC) measurements, including photocurrent response, electrochemical impedance spectra (EIS), and open circuit potential decay curves (OCP), further supported the Z-scheme mechanism. The novelty of this work is to provide atomic precision of the interfacial heterojunction for further research in this area.

7.4 BP/RP-QD Z-scheme heterojunction

In the same year, Shi *et al.* proposed a Z-scheme based BP/RP-QD heterojunction with varying wt% of Co (co-catalyst) *via* a wet-chemistry reflux approach for H_2 generation without a sacrificial agent.[202] Ethylenediamine solvent plays a vital role in the *in situ* phase change of RP to BP. The HRTEM analysis

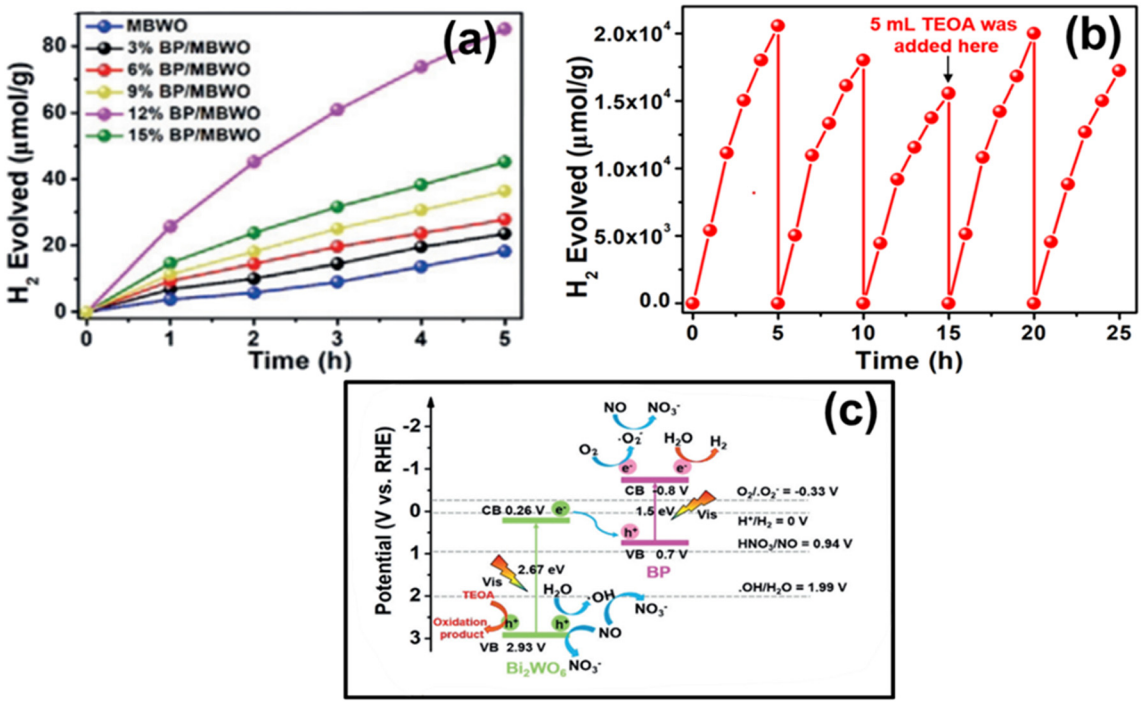

Fig. 9 (a) The production of H_2 gas through photocatalysis utilizing various photocatalysts, (b) stability plot for the production of H_2 using the 12% BP/MBWO catalyst, and (c) scheme illustrating the potential photocatalytic reaction and the flow of charges along the Z-scheme pathway enabled by the BP/MBWO catalyst. Adapted with permission.[200] Copyright 2018, Wiley.

confirmed the quantum size (7 ± 3 nm) distribution of BP and RP in the composite. The maximum activity was observed for the 2 wt% Co-loaded BP/RP-QD composite, *i.e.*, 3660 µmol g^{-1} h^{-1}, as shown in Fig. 11a, and AQE of about 1.53% (420 nm). In contrast, the system retained about 71% activity even after four cycles (12 hours) as depicted in Fig. 11b. The quantum confinement demonstrated the Z-scheme mechanism instead of the type-I heterostructure mechanism between the junction of BP & RP (Fig. 11c). Subsequently, it enables the BP/RP heterostructure to perform photocatalytic water splitting.

Furthermore, the active redox potential and effective separation of photoproduced excitons *via* the Z-scheme path were depicted by overlapping the cathodic photocurrent of BP-QD with the anodic photocurrent of RP-QD. By tracing the kinetics of photogenerated charge carriers *via* TAS, the group confirmed the direct CT mechanism between BP & RP *via* the Z-scheme pathway. Moreover, the *in situ* EPR spectra enable the detection of hydroxyl radicals of 2 wt% Co–BP/RP-QD which was confirmed by the use of PL spectra as shown in Fig. 11b and c, respectively. This work constructed a pathway for effective overall water splitting under solar light illumination to avoid photo corrosion of BP/RP-QD.

7.5 NYF/Ag_3PO_4/BP ternary heterostructure

The Z-scheme composite is considered an advantageous photocatalytic system, but the development of NIR active systems is very low. Therefore, for the transformation of low-energy NIR light into high-energy UV and visible light, a lanthanide doped (Yb^{3+}, Tm^{3+}) direct Z-scheme NYF/Ag_3PO_4/BP heterostructure was fabricated for the first time by Zhang and collaborators in 2019.[203] When exposed to 980 nm laser light, the up-conversion material $NaYF_4$:Yb^{3+}, Tm^{3+} (NYF) converted into a visible and ultraviolet active system, in which Ag_3PO_4 and BP were utilized to generate photoexcited charge carriers. On the other hand, when pure Ag_3PO_4 was exposed to 980 nm laser light, it demonstrated no photocatalytic activity, whereas both BP and NYF/BP exhibited low H_2 production under the same conditions. The optimum H_2 production was observed to be 8.756 µmol (4 hours) for NYF/Ag_3PO_4/BP-2 without using any co-catalyst. However, among various sacrificial agents like methanol and TEOA, the use of glycerol (50 vol% GLY) depicts maximum H_2 generation, *i.e.*, 145.93 µmol h^{-1} g^{-1} (10.2 times and 6.1 times more significant compared to pure BP and NYF/BP respectively) as shown in Fig. 12a and an AQE of about 0.077%, respectively. Further, the catalyst remained stable for five consecutive cycles without any noticeable reduction in efficiency (Fig. 12b). The electrons on the CB of BP carry out the reduction reaction. In contrast, hydroxyl radicals (˙OH) are produced owing to the oxidation facilitated by the holes present in the VB of Ag_3PO_4. Furthermore, the Yb^{3+} ion utilized as a sensitizer, which was excited by the use of 980 nm laser light irradiation, successively transmitted the energy to adjacent Tm^{3+}, determining the possibility of a Z-scheme mechanism as displayed in Fig. 12c. The enhanced photocatalytic performance *via* Z-scheme electron migration has been verified through surface redox reactions and electron spin resonance (ESR)

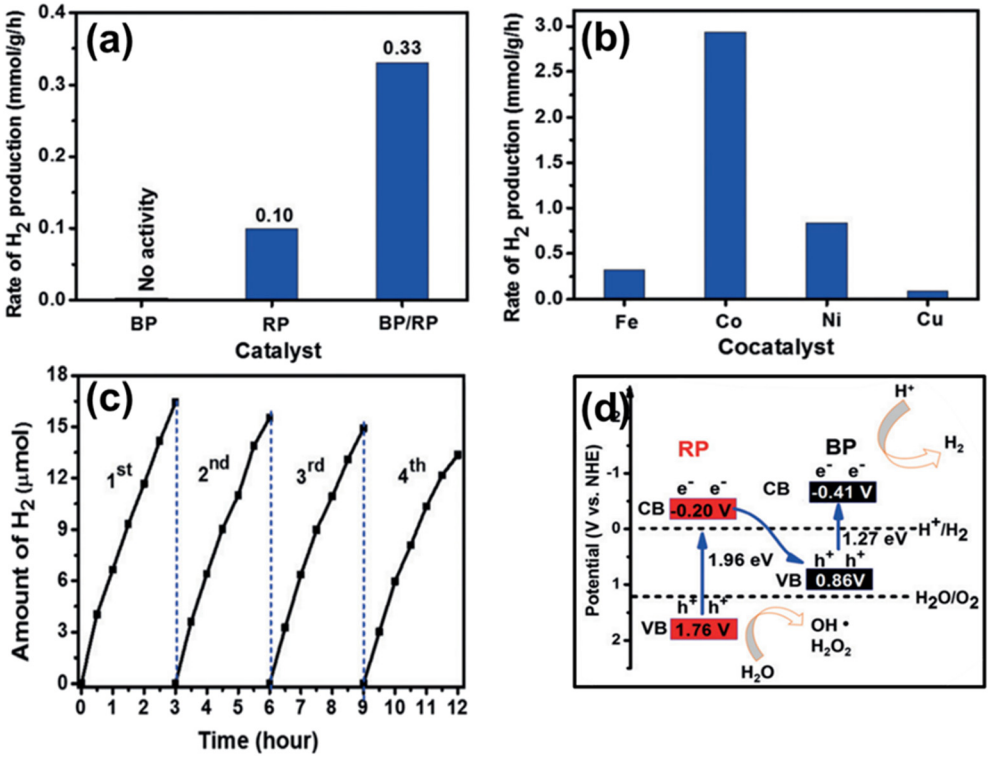

Fig. 10 (a) The rate of H_2 evolution through photocatalysis employing various samples, (b) the H_2 evolution rate over the BP/RP heterojunction with the inclusion of different non-noble metals, and (c) an assessment of photocatalytic stability, (d) the energy band structure, and the pathway for interfacial Z-scheme CT within the BP/RP heterostructure.[201] Copyright 2019, Wiley.

spectra. In brief, the team demonstrated this work for the future generation towards a new pathway for developing NIR-light-induced Z-scheme photocatalysts.

7.6 BP/WN heterojunction

Xu *et al.* first developed a noble-metal free NIR active Z-scheme based 2D/2D BP–BM/WN heterojunction (ball milling method) photocatalyst and examined it for H_2 evolution activity.[204] They found that the composite shows an optimum H_2 production rate of 10.77 μmol h^{-1} g^{-1} (12* BP–BM and 108* WN) under NIR light and 18 842 μmol h^{-1} g^{-1} under visible light in the absence of a co-catalyst and sacrificial agent as shown in Fig. 13a. The composite exhibits excellent photostability up to 15 h ($\lambda \geq 700$ nm) with minute reduction in performance as depicted in Fig. 13b. This outstanding improvement in activity compared to pristine materials corresponds to effective separation and a longer lifespan of photoexcited carriers *via* the proposed 2D/2D Z-scheme heterojunction (Fig. 13c). The successive exciton segregation is well studied by electrochemical and TRPL measurements. Further, the inter-crossing of lattice fringes of WN (200) and BP (040) sheets demonstrates heterostructure formation and is well supported by XRD, Raman, and XPS analysis. The team observed that the ultrathin BP obtained *via* ball milling is the cause of increased activity but somehow reduces the crystallinity. Further, from theoretical (DFT) and experimental (UPS and MS) measurements, the group calculated the band edge potential and proved the metallic character of the WN unit. Additionally, the calculated AQE over the BP–BM/WN hybrid is 0.24% at λ ~800 nm, and the projected Z-scheme mechanism is validated *via* photoelectrochemical analysis. Hence, this approach demonstrated new ideas on noble metal-free NIR active Z-scheme based heterojunctions for enhanced solar-energy conversion.

7.7 BP/$ZnFe_2O_4$ heterostructure

Wang and co-workers developed a core–shell heterostructure called $ZnFe_2O_4$/BP (ZFO–BP) for H_2 production.[205] They achieved the highest hydrogen generation rates (without co-catalyst) of 2160 μmol h^{-1} g^{-1} and 560 μmol h^{-1} g^{-1} respectively, under solar light and NIR light ($\lambda > 820$ nm) illumination, as shown in Fig. 14a. This was accompanied by an AQE of 1.62% at a wavelength of 820 nm. Furthermore, the formation of the Zn–P linkage (i) enhanced the bond strength between ZFO and BP, (ii) promoted the effective CT *via* generating carrier migration channels and active reaction sites, (iii) the 3D microcavity structure supported multiple light reflections within the catalyst, and (iv) it optimized the Gibbs free energy of BP by modulating its electronic configuration. The photocatalytic stability of the ZFO–BP core–shell hybrid maintained almost 95% of activity even after four cycles (Fig. 14b). The stability of the photocatalyst was also confirmed during a one-month storage period, with no significant changes in crystal structure observed through XRD and SEM analysis. Moreover, the proposed Z-scheme mechanism (justified by XPS and EPR analysis) illustrated in

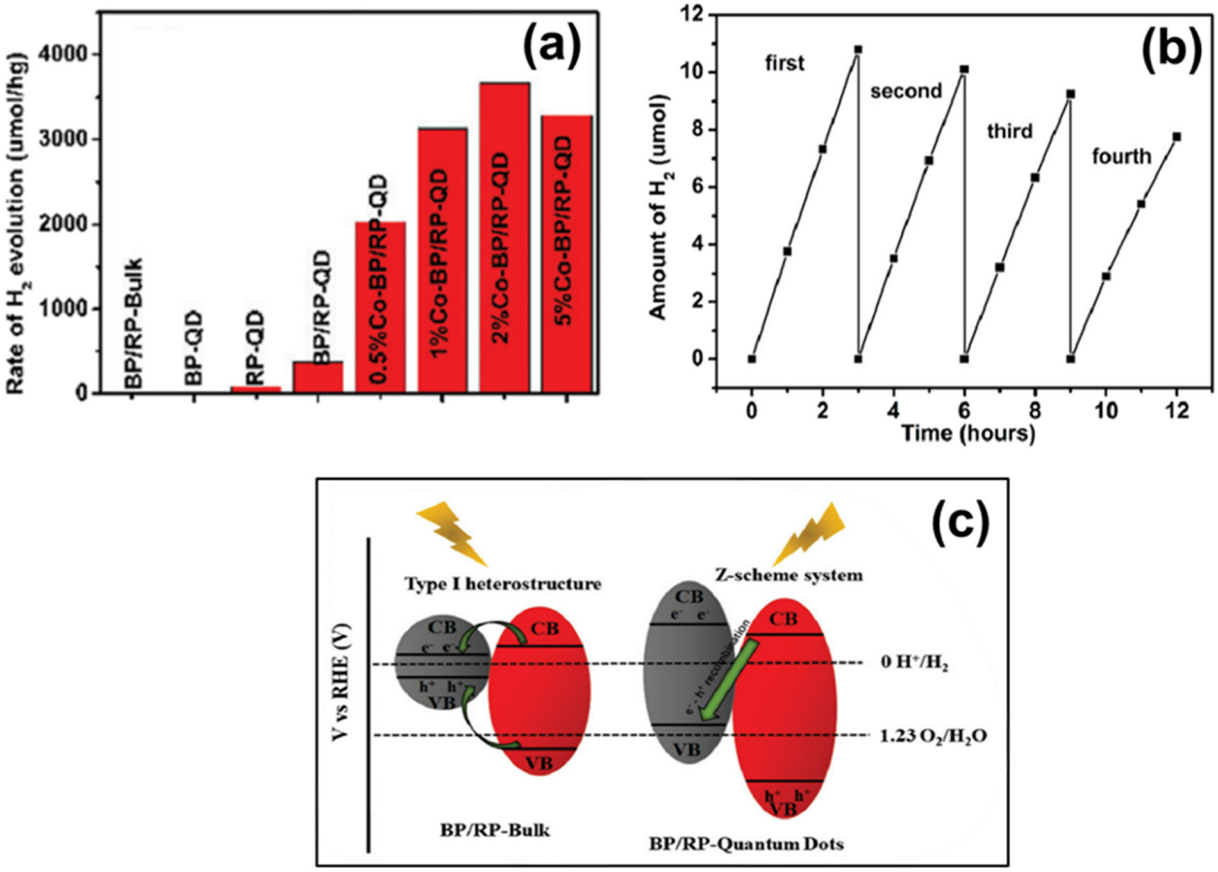

Fig. 11 (a) The rate of solar H_2 evolution across different samples, (b) an assessment of the reusability test of 2 wt% Co–BP/RP-QD, and (c) a schematic depiction of the energy level arrangements within BP/RP-bulk and a representation of the charge flow along the Z-scheme pathway facilitated by the BP/RP-QD catalyst. Adapted with permission.[202] Copyright 2019, The Royal Society of Chemistry.

Fig. 14c demonstrated the successful construction of Zn–P ET between ZFO and BP, which improved the carrier transfer property, redox potential, and adsorption–desorption balance of BP. Additionally, HRTEM images confirmed the close lattice contact between ZFO and BP NSs, affirming the formation of a high-quality heterojunction. This improved the sunlight reflection within ZFO–BP and enhanced the availability of reaction active sites during photocatalytic reactions. When compared to a mixture of ZFO and BP under the same conditions, the ZFO–BP heterostructure exhibited significantly enhanced photocatalytic activity, emphasizing the crucial role of Zn–P bonds in this improvement. Additionally, the formation of Zn–P bonds was found to enhance carrier transfer properties, as confirmed through DFT calculations, X-ray absorption spectra (XAS), Raman, and XPS spectra. In summary, the suggested photocatalytic processes, supported by a sequence of experimental analyses and theoretical calculations, can potentially develop more effective and enduring photocatalysts using BP for current energy conversion purposes.

7.8 BP/Fe_2O_3 binary heterojunction

Utilizing a Z-scheme photocatalytic system that involves an O_2 production photocatalyst (OPP) and an H_2 production photocatalyst (HPP) holds great potential for productive solar to-chemical conversion. In this regard, Shi and team (2021), for the first time, designed a cost-effective all solid-state 2D–2D BP/α-Fe_2O_3 Z-scheme system of different BP wt%. The composite was tested for H_2 and O_2 production without the support of any hole or electron sacrificial agent, where 2D BP NSs acted as a HPP and α-Fe_2O_3 served as an OPP, respectively.[206] Moreover, BP NSs acting as a solid-state mediator get interlinked with α-Fe_2O_3 through strong interaction, improving the photocatalytic activity by promoting the separation and the migration of excitons *via* Z-scheme charge dynamics. Electrochemical measurements show that incorporating 2D BP enhances the separation and movement of photogenerated carriers between 2D BP and α-Fe_2O_3. This heterostructure demonstrated a remarkable 7.4-fold increase in photocatalytic activity compared to the performance of bare 2D BP alone. Additionally, the overall H_2 generation of the 15 wt% BP/α-Fe_2O_3 (P–FO) nanocomposite was found to be 0.59 μmol h^{-1}, under the influence of visible light illumination (300 W Xe lamp) using CO_3O_4 and Pt as co-catalysts (Fig. 15a), which remained stable for three cyclic runs (15 hours) as shown in Fig. 15b. To clarify the Z-scheme mechanism of the

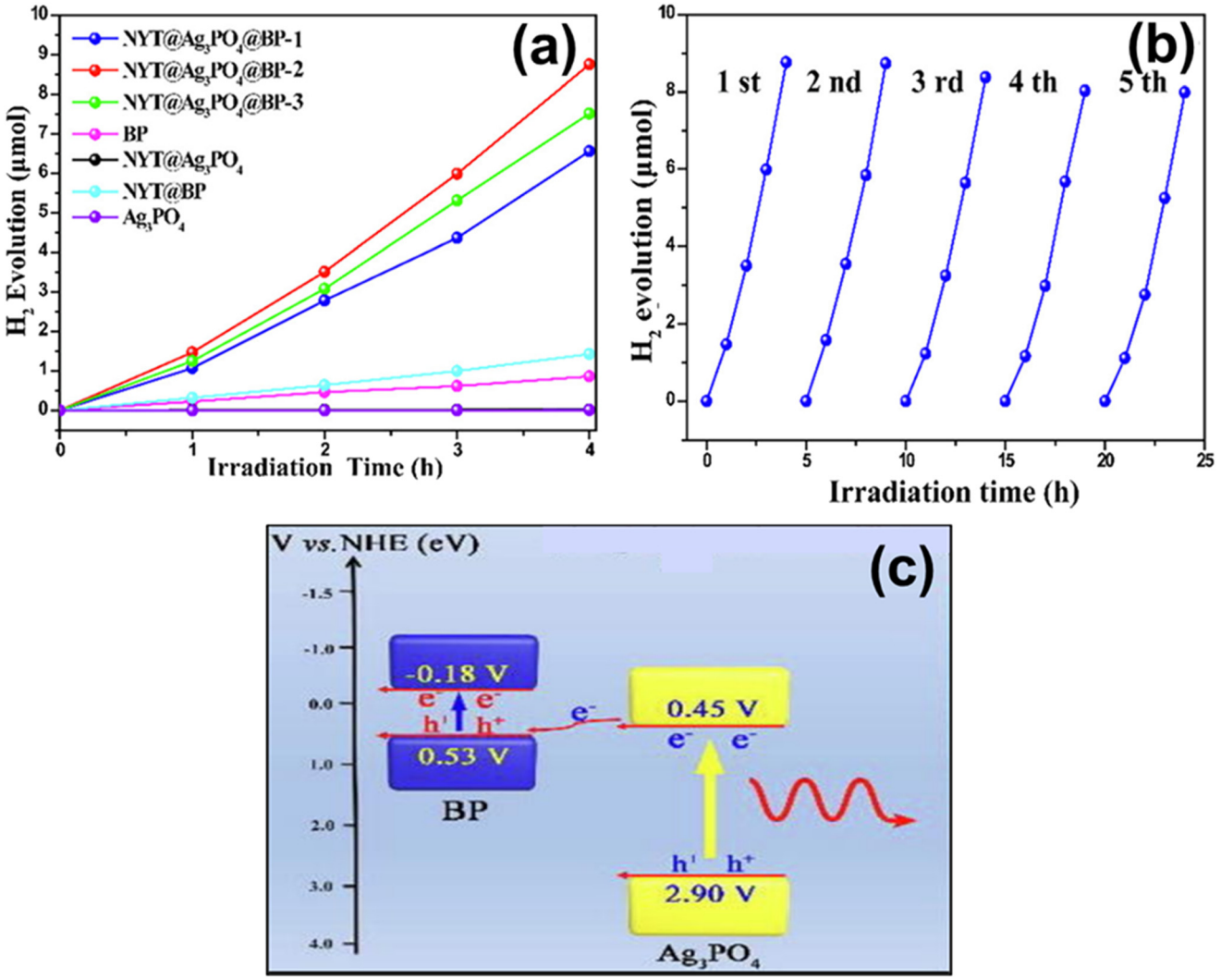

Fig. 12 (a) Depiction of photo-induced catalytic H_2 production using sacrificial agents (glycerol), (b) evaluation of the durability of NYF/Ag_3PO_4/BP-2 for the photocatalytic generation of H_2 gas, and (c) plausible mechanism towards solar H_2 gas production by the NYF/Ag_3PO_4/BP ternary heterostructure. Adapted with permission.[203] Copyright 2019, Elsevier.

BP/α-Fe_2O_3 heterostructure, spin-trapping ESR scanning was conducted. The DMPO–˙OH spin-trapping ESR spectral analysis results supported the formation of a 2D–2D Z-scheme BP/α-Fe_2O_3 heterojunction rather than a type-II heterojunction (Fig. 15c). Further, the photocurrent measurement and EIS spectra supported the most effective photoexcited e^-–h^+ separation over 15 wt% P–FO compared to other prepared systems. In brief, utilizing the cost-effective and eco-friendly BP/α-Fe_2O_3 heterostructure can achieve improved water splitting performance, opening up new possibilities for energy conversion related applications.

7.9 BP/MoO_{3-x} binary composite

Herein, Fan and colleagues introduced a novel binary composite, BP/MoO_{3-x}, using a facile ball milling approach to enhance the production of H_2 gas.[207] They found that when BP coupled with plasmonic MoO_{3-x} in a 1 : 1 weight ratio, it significantly increased the rate of H_2 generation, reaching 396.3 μmol h^{-1} g^{-1} under visible light and 156.4 μmol h^{-1} g^{-1} under NIR photon irradiation. This was a substantial improvement of approximately 40 and 80 times, respectively compared to bare BP without using any sacrificial chemicals, as shown in Fig. 16a. The BP/MoO_{3-x} heterostructure demonstrated excellent stability when exposed to visible light for five consecutive cycles (25 hours), with no significant decrease in photocatalytic performance (Fig. 16b). Furthermore, even after being stored in an argon (Ar) atmosphere for a month, the BP/MoO_{3-x} photocatalyst retained its original activity, indicating its suitability as a stable photocatalyst for H_2 production. The study employed density functional theory (DFT) calculations to analyse the synergistic effect of the Z-scheme BP/MoO_{3-x} heterostructure. They also harnessed the strong localized surface plasmon resonance (LSPR) to enhance light

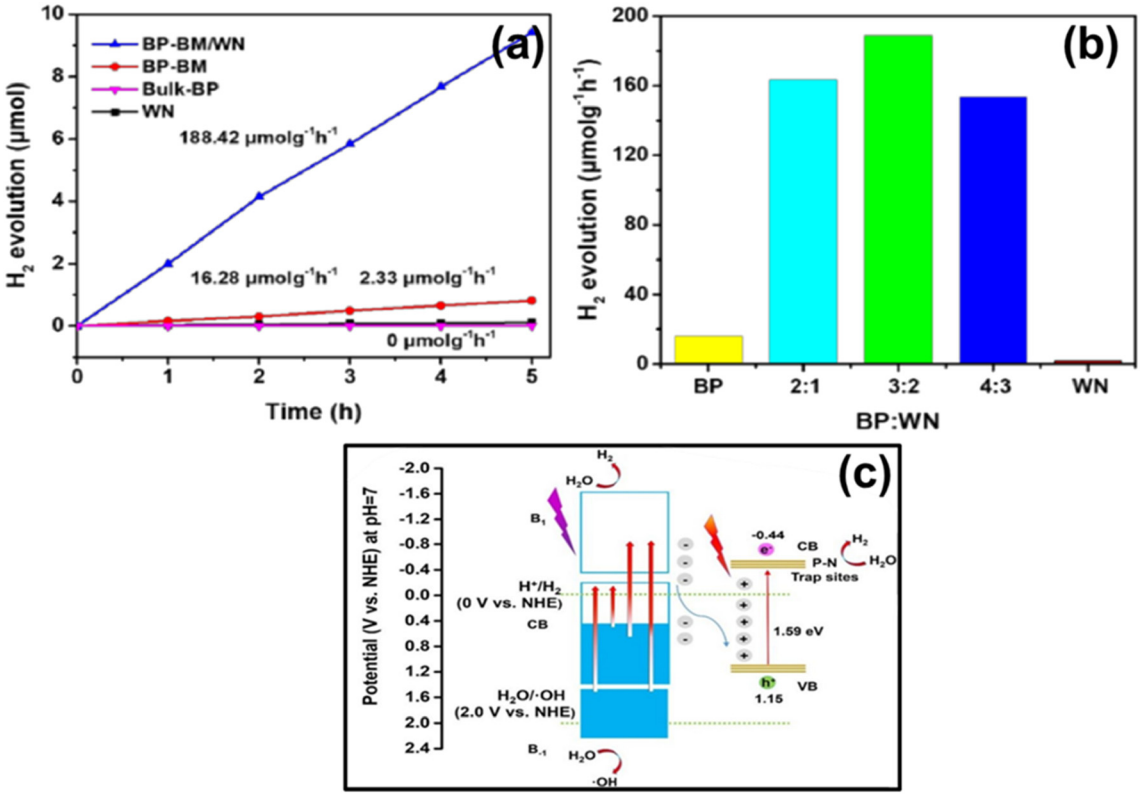

Fig. 13 (a) The production of H_2 gas through photocatalysis using various catalysts in deionized water, (b) a test to assess the stability of the BP–BM/WN heterostructure for photocatalytic H_2 evolution over multiple cycles under irradiation from light exceeding 700 nm, and (c) a visual representation of the Z-scheme mechanism towards solar H_2 evolution by the BP–BM/WN heterostructure. Adapted with permission.[204] Copyright 2020, Elsevier.

absorption, subsequently improving the efficiency of separating/ transferring photo-generated charge carriers. Additionally, coupling BP with defective plasmonic MoO_{3-x} through a Mo–P covalent bond enabled efficient photon

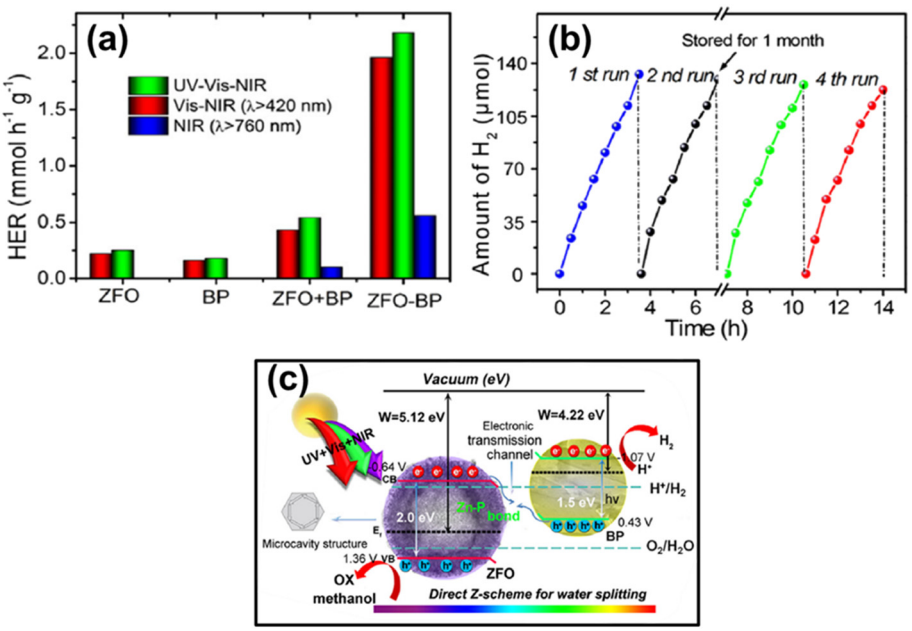

Fig. 14 (a) The photocatalytic performance in generating H_2 gas using various samples, (b) the cyclic stability test of ZFO–BP samples over four consecutive cycles, and (c) a schematic illustration of the Z-scheme within the core–shell ZFO–BP microcavity structure. Adapted with permission.[205] Copyright 2021, Elsevier.

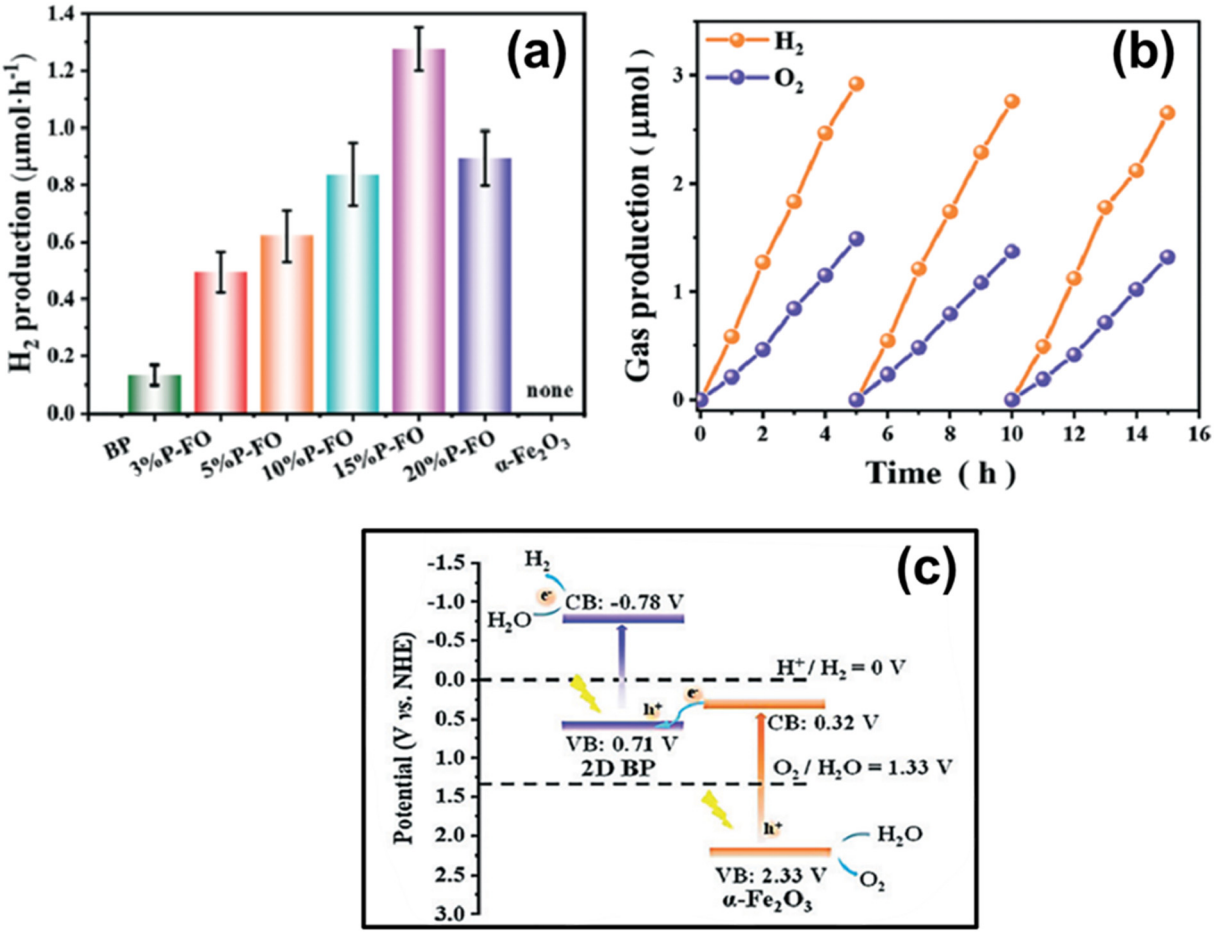

Fig. 15 (a) The rate of H_2 generation observed by using various photocatalysts, (b) a test evaluating the long-term stability of the 15% P–FO photocatalyst, and (c) a schematic depiction of the mechanistic approach towards the Z-scheme system facilitated by the BP/α-Fe_2O_3 heterostructure. Adapted with permission.[206] Copyright 2020, The Royal Society of Chemistry.

harvesting from the visible to NIR range. This facilitated the effective separation of photo-generated excitons *via* the Z-scheme transfer pathway (Fig. 16c), which was demonstrated through PL, TRPL, EIS measurements, and transient photocurrent responses. In summary, the study aimed to highlight the advantageous characteristics of the newly synthesized Z-scheme charge migration and confirmatory characterization techniques for developing heterostructured photocatalysts in the context of solar energy conversion and H_2 production, particularly in the NIR part of the electromagnetic spectrum.

8. Conclusion and future prospective

Recently, BP has emerged as a highly promising semiconductor photocatalyst with different dimensional structures owing to its unique optoelectronic properties. This review comprises a brief encyclopedia of BP and its modified systems in the arena of photocatalytic H_2 evolution through water splitting mainly:

- Complete overview of BP, encompassing the fabrication methods of various morphology-oriented BP and its modified systems across multiple dimensions, mostly bulk, 2D NSs, and 0D QDs. Moreover, various optoelectronic and photocatalytic features, like crystal structure, band structure, and anisotropy, along with the stability of BP are well explained.
- Various types of CT mechanisms like type-II, traditional, and modified Z-scheme based heterostructures are briefly elaborated.
- The case study of various photocatalytic H_2 evolution reactions undergoing the Z-scheme CT mechanism is explained in detail.

However, many unexplored highlights need to be addressed for achieving a benchmark activity in solar fuel production using BP-based photocatalytic systems:

1) *In situ* techniques offer real-time monitoring and quantitative data that help elucidate the mechanisms behind the catalytic processes occurring on BP-based heterojunctions. *In situ* characterization techniques such as XPS, FTIR, DRIFT, Raman spectroscopy, and femtosecond

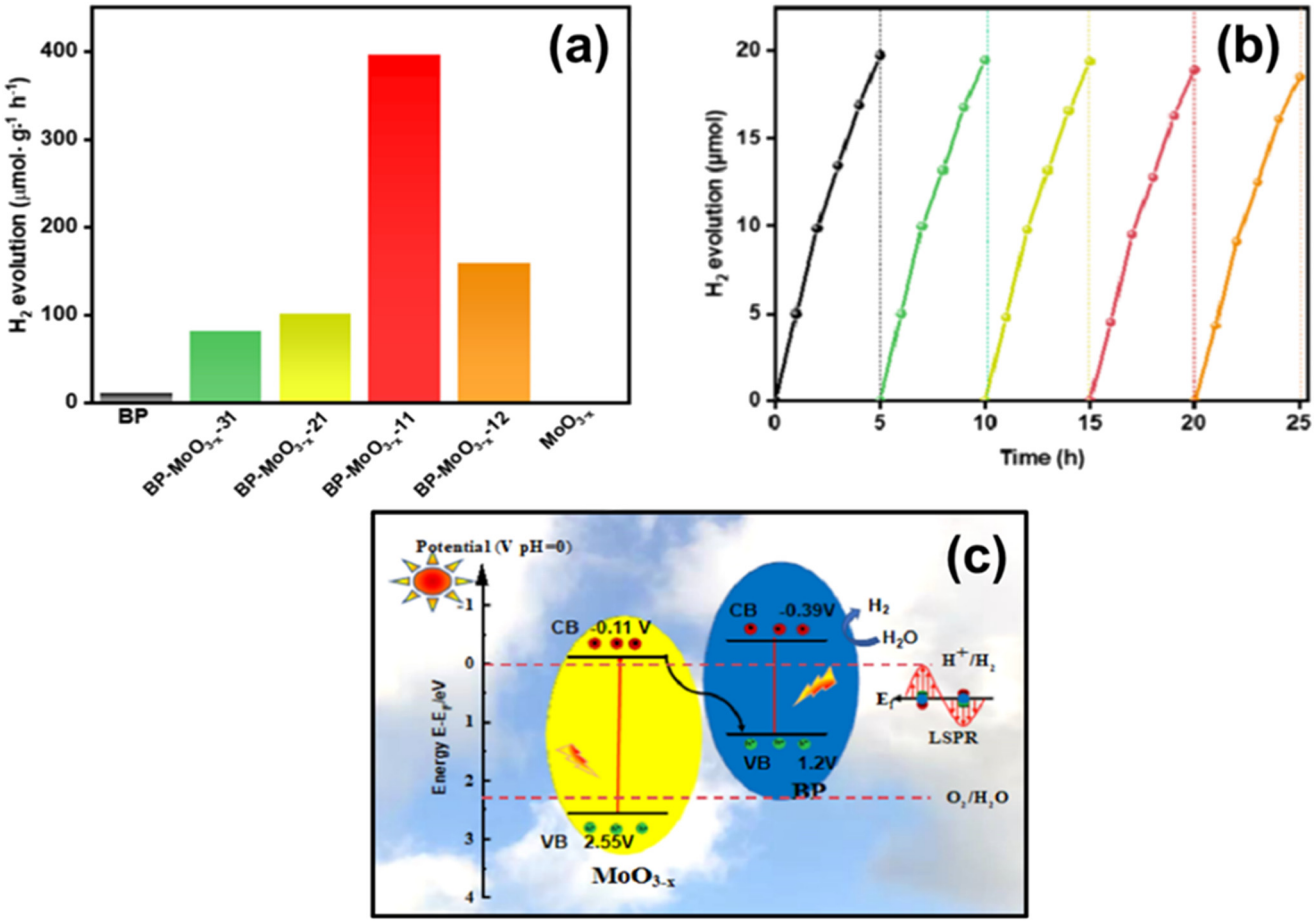

Fig. 16 (a) The rate of H_2 evolution with varying ratios of BP to MoO_{3-x} in the feed, (b) the durability and consistency of photocatalytic H_2 gas production using the BP/MoO_{3-x}-11 heterostructure, and (c) the mechanism underlying the photocatalytic production of H_2 gas employing the BP/MoO_{3-x} heterostructure. Adapted with permission.[207] Copyright 2022, American Chemical Society.

time-resolved transient absorption spectroscopy, as well as techniques like photo-illuminated Kelvin probe analysis offer essential insight into the performed catalytic processes of BP-based heterojunctions that need to be explored to uncover the underlying catalytic mechanism.

2) Despite having excellent optoelectronic features, the application of BP-based systems is still in the infant stage in the arena of photocatalytic, electrocatalytic, and piezo/pyro photocatalytic N_2 reduction, H_2O_2 production, CO_2 reduction, pollutant abatement, valorisation reaction, and organic transformation reaction. Achieving large-scale production while maintaining quality is a challenge. Hence, scalable synthesis methods for high-quality BP materials are essential for practical applications.

3) Computational machine learning techniques might guide the construction of highly active BP-based heterojunction photocatalysts. It is an effective method that enables the targeted prediction and selection of photocatalysts with desired properties from sizable prebuilt databases. It includes catalyst band structures, work functions, composite binding energies, interfacial interactions, and energy variations in redox reactions over the surface.

4) By integrating experimental data with theoretical DFT computations and leveraging machine learning techniques, researchers can gain a deeper understanding of the underlying mechanisms governing the photocatalytic properties of BP-based systems. This holistic approach enables the design of highly efficient and promising photocatalytic materials for various applications, from environmental remediation to energy conversion. Machine learning algorithms can help establish quantitative relationships between experimental outcomes and theoretical parameters, facilitating the prediction of photocatalytic activity based on material properties.

5) Manufacturing of laboratory and industrial grade BP-based systems without compromising the inherent properties with high stability can be achieved. BP is known to be sensitive to moisture and air, which can lead to degradation. New strategies to stabilize BP, such as encapsulation in protective layers or using passivation techniques, were developed. This will help maintain the stability of the material over time. A robust quality assurance program should be implemented to monitor and maintain the quality of the manufactured systems. This includes regular testing,

inspection, and process optimization. As with any emerging technology, safety and environmental considerations must be addressed when working with BP-based materials, especially in industrial applications.

Conflicts of interest

The authors declare no competing financial interest.

Acknowledgements

The authors express their profound gratitude toward Siksha 'O' Anusandhan (Deemed to be University) management for providing necessary facilities and consistent encouragement.

References

1 E. Gong, S. Ali, C. B. Hiragond, H. S. Kim, N. S. Powar, D. Kim, H. Kim and S. Il In, *Energy Environ. Sci.*, 2021, **15**, 880–937.
2 M. Z. Hussain, Z. Yang, Z. Huang, Q. Jia, Y. Zhu and Y. Xia, *Adv. Sci.*, 2021, **8**, 2100625.
3 G. Zhang, H. Wu, D. Chen, N. Li, Q. Xu, H. Li, J. He and J. Lu, *Green Energy Environ.*, 2022, **7**, 176–204.
4 Y. Ren, D. Zeng and W. J. Ong, *Chin. J. Catal.*, 2019, **40**, 289–319.
5 J. Yang, H. Wang, L. Jiang, H. Yu, Y. Zhao, H. Chen, X. Yuan, J. Liang, H. Li and Z. Wu, *Chem. Eng. J.*, 2022, **427**, 130991.
6 B. Zhu, B. Cheng, J. Fan, W. Ho and J. Yu, *Small Struct.*, 2021, **12**, 2100086.
7 Z. Wang, Z. Lin, S. Shen, W. Zhong and S. Cao, *Chin. J. Catal.*, 2021, **42**, 710–730.
8 K. C. Christoforidis and P. Fornasiero, *ChemCatChem*, 2017, **9**, 1523–1544.
9 C. Wang and D. Astruc, *Chem. Soc. Rev.*, 2014, **43**, 7188–7216.
10 M. Ohashi, M. Aoki, K. I. Yamanaka, K. Nakajima, T. Ohsuna, T. Tani and S. Inagaki, *Chem. – Eur. J.*, 2009, **15**, 13041–13046.
11 L. Wang, J. Zhang, Y. Zhang, H. Yu, Y. Qu and J. Yu, *Small*, 2022, **18**, 2104561.
12 C. Xia, H. Wang, J. K. Kim and J. Wang, *Adv. Funct. Mater.*, 2021, **31**, 2008247.
13 J. Wang, S. Lin, N. Tian, T. Ma, Y. Zhang and H. Huang, *Adv. Funct. Mater.*, 2021, **31**, 2008008.
14 X. Wu, S. Xie, H. Zhang, Q. Zhang, B. F. Sels and Y. Wang, *Adv. Mater.*, 2021, **33**, 2007129.
15 K. Maeda, T. Takata, M. Hara, N. Saito, Y. Inoue, H. Kobayashi and K. Domen, *J. Am. Chem. Soc.*, 2005, **127**, 8286–8287.
16 J. Liao, B. Sa, J. Zhou, R. Ahuja and Z. Sun, *J. Phys. Chem. C*, 2014, **118**, 17594–17599.
17 G. Z. S. Ling, S. F. Ng and W. J. Ong, *Adv. Funct. Mater.*, 2022, **32**, 2111875.
18 X. Yang, Y. Ye, J. Sun, Z. Li, J. Ping and X. Sun, *Small*, 2022, **18**, 2105089.
19 J. Wang and S. Wang, *Coord. Chem. Rev.*, 2022, **453**, 214338.
20 Y. Guan, Y. Liu, Q. Lv and J. Wu, *J. Hazard. Mater.*, 2021, **418**, 126280.
21 H. Ma, Y. He, P. Chen, H. Wang, Y. Sun, J. Li, F. Dong, G. Xie and J. Sheng, *Chem. Eng. J.*, 2021, **417**, 129305.
22 L. Zhang, Y. Li, Q. Li, J. Fan, S. A. C. Carabineiro and K. Lv, *Chem. Eng. J.*, 2021, **419**, 129484.
23 X. Zhang, S. Tong, D. Huang, Z. Liu, B. Shao, Q. Liang, T. Wu, Y. Pan, J. Huang, Y. Liu, M. Cheng and M. Chen, *Coord. Chem. Rev.*, 2021, **448**, 214177.
24 Y. C. Wang, X. Y. Liu, X. X. Wang and M. S. Cao, *Chem. Eng. J.*, 2021, **419**, 129459.
25 M. Guo, M. Zhang, R. Liu, X. Zhang and G. Li, *Adv. Sci.*, 2022, **9**, 2103361.
26 X. Zhang, R. Tang, F. Li, R. Zheng and J. Huang, *Sol. RRL*, 2022, **6**, 2101058.
27 P. W. Bridgman, *J. Am. Chem. Soc.*, 1914, **36**, 1344–1363.
28 X. Zhu, J. Yang, X. She, Y. Song, J. Qian, Y. Wang, H. Xu, H. Li and Q. Yan, *J. Mater. Chem. A*, 2019, **7**, 5209–5213.
29 X. Zhu, S. Huang, Q. Yu, Y. She, J. Yang, G. Zhou, Q. Li, X. She, J. Deng, H. Li and H. Xu, *Appl. Catal., B*, 2020, **269**, 118760.
30 H. You, Y. Jia, Z. Wu, F. Wang, H. Huang and Y. Wang, *Nat. Commun.*, 2018, **9**, 2889.
31 S. Pan, J. He, C. Wang and Y. Zuo, *Mater. Lett.*, 2018, **212**, 311–314.
32 M. Z. Rahman, C. W. Kwong, K. Davey and S. Z. Qiao, *Energy Environ. Sci.*, 2016, **9**, 709–728.
33 Y. J. Yuan, S. Yang, P. Wang, Y. Yang, Z. Li, D. Chen, Z. T. Yu and Z. G. Zou, *Chem. Commun.*, 2018, **54**, 960–963.
34 V. Tran, R. Soklaski, Y. Liang and L. Yang, *Phys. Rev. B: Condens. Matter Mater. Phys.*, 2014, **89**, 235319.
35 H. Liu, Y. Du, Y. Deng and P. D. Ye, *Chem. Soc. Rev.*, 2015, **44**, 2732–2743.
36 J. Pang, A. Bachmatiuk, Y. Yin, B. Trzebicka, L. Zhao, L. Fu, R. G. Mendes, T. Gemming, Z. Liu and M. H. Rummeli, *Adv. Energy Mater.*, 2018, **8**, 1702093.
37 L. Li, Y. Yu, G. J. Ye, Q. Ge, X. Ou, H. Wu, D. Feng, X. H. Chen and Y. Zhang, *Nat. Nanotechnol.*, 2014, **9**, 372–377.
38 J. R. Brent, N. Savjani, E. A. Lewis, S. J. Haigh, D. J. Lewis and P. O'Brien, *Chem. Commun.*, 2014, **50**, 13338–13341.
39 A. Castellanos-Gomez, L. Vicarelli, E. Prada, J. O. Island, K. L. Narasimha-Acharya, S. I. Blanter, D. J. Groenendijk, M. Buscema, G. A. Steele, J. V. Alvarez, H. W. Zandbergen, J. J. Palacios and H. S. J. Van Der Zant, *2D Mater.*, 2014, **1**, 025001.
40 X. Zhu, T. Zhang, Z. Sun, H. Chen, J. Guan, X. Chen, H. Ji, P. Du and S. Yang, *Adv. Mater.*, 2017, **29**, 1605776.
41 Y. J. Yuan, J. R. Tu, Z. J. Ye, D. Q. Chen, B. Hu, Y. W. Huang, T. T. Chen, D. P. Cao, Z. T. Yu and Z. G. Zou, *Appl. Catal., B*, 2016, **188**, 13–22.
42 Y. J. Yuan, Z. J. Ye, H. W. Lu, B. Hu, Y. H. Li, D. Q. Chen, J. S. Zhong, Z. T. Yu and Z. G. Zou, *ACS Catal.*, 2016, **6**, 532–541.
43 Y. J. Yuan, Z. Shen, S. Wu, Y. Su, L. Pei, Z. Ji, M. Ding, W. Bai, Y. Chen, Z. T. Yu and Z. Zou, *Appl. Catal., B*, 2019, **246**, 120–128.

44 Y. J. Yuan, Z. Li, S. Wu, D. Chen, L. X. Yang, D. Cao, W. G. Tu, Z. T. Yu and Z. G. Zou, *Chem. Eng. J.*, 2018, **350**, 335–343.
45 M. Zhu, C. Zhai, M. Fujitsuka and T. Majima, *Appl. Catal., B*, 2018, **221**, 645–651.
46 Q. Liang, F. Shi, X. Xiao, X. Wu, K. Huang and S. Feng, *ChemCatChem*, 2018, **10**, 2179–2183.
47 Y. Abate, D. Akinwande, S. Gamage, H. Wang, M. Snure, N. Poudel and S. B. Cronin, *Adv. Mater.*, 2018, **30**, 1704749.
48 Z. Guo, S. Chen, Z. Wang, Z. Yang, F. Liu, Y. Xu, J. Wang, Y. Yi, H. Zhang, L. Liao, P. K. Chu and X. F. Yu, *Adv. Mater.*, 2017, **29**, 1703811.
49 J. Kou, C. Lu, J. Wang, Y. Chen, Z. Xu and R. S. Varma, *Chem. Rev.*, 2017, **117**, 1445–1514.
50 Y. Huang, H. Lu, B. Wang, W. He, H. Dong, L. Sui, Z. Gan, S. Ma, B. Pang, L. Dong and L. Yu, *Int. J. Hydrogen Energy*, 2021, **46**, 3530–3538.
51 S. Zhao, J. Wu, K. Jin, H. Ding, T. Li, C. Wu, N. Pan and X. Wang, *Adv. Funct. Mater.*, 2018, **28**, 1802011.
52 N. Liang, M. Wang, L. Jin, S. Huang, W. Chen, M. Xu, Q. He, J. Zai, N. Fang and X. Qian, *ACS Appl. Mater. Interfaces*, 2014, **6**, 11698–11705.
53 M. Yu, H. Liang, R. Zhan, L. Xu and J. Niu, *Chin. Chem. Lett.*, 2021, **32**, 2155–2158.
54 M. Zhu, S. Kim, L. Mao, M. Fujitsuka, J. Zhang, X. Wang and T. Majima, *J. Am. Chem. Soc.*, 2017, **139**, 13234–13242.
55 M. Wen, J. Wang, R. Tong, D. Liu, H. Huang, Y. Yu, Z. K. Zhou, P. K. Chu and X. F. Yu, *Adv. Sci.*, 2019, **6**, 1801321.
56 T. Song, G. Zeng, P. Zhang, T. Wang, A. Ali, S. Huang and H. Zeng, *J. Mater. Chem. A*, 2019, **7**, 503–512.
57 W. Lei, Y. Mi, R. Feng, P. Liu, S. Hu, J. Yu, X. Liu, J. A. Rodriguez, J. ou Wang, L. Zheng, K. Tang, S. Zhu, G. Liu and M. Liu, *Nano Energy*, 2018, **50**, 552–561.
58 O. Elbanna, M. Zhu, M. Fujitsuka and T. Majima, *ACS Catal.*, 2019, **9**, 3618–3626.
59 J. Ran, X. Wang, B. Zhu and S. Z. Qiao, *Chem. Commun.*, 2017, **53**, 9882–9885.
60 Y. Wang, J. Wu, Y. Yan, L. Li, P. Lu, J. Guan, N. Lu and X. Yuan, *Chem. Eng. J.*, 2021, **403**, 126313.
61 R. Guan, L. Wang, D. Wang, K. Li, H. Tan, Y. Chen, X. Cheng, Z. Zhao, Q. Shang and Z. Sun, *Chem. Eng. J.*, 2022, **435**, 135138.
62 R. Wang, M. Zhang, B. Ge, L. Zhang, J. Zhou, S. Liu and T. Jiao, *J. Mol. Liq.*, 2020, **310**, 113083.
63 P. Qiu, C. Xu, N. Zhou, H. Chen and F. Jiang, *Appl. Catal., B*, 2018, **221**, 27–35.
64 Y. Hong, Y. Jiang, C. Li, W. Fan, X. Yan, M. Yan and W. Shi, *Appl. Catal., B*, 2016, **180**, 663–673.
65 H. Du, X. Lin, Z. Xu and D. Chu, *J. Mater. Chem. C*, 2015, **3**, 8760–8775.
66 T. Kikegawa and H. Iwasaki, *Acta Crystallogr., Sect. B: Struct. Sci.*, 1983, **39**, 158–164.
67 J. C. Jamieson, *Science*, 1963, **139**, 1291–1292.
68 Y. Du, C. Ouyang, S. Shi and M. Lei, *J. Appl. Phys.*, 2010, **107**, 093718.
69 L. Seixas, A. S. Rodin, A. Carvalho and A. H. Castro Neto, *Phys. Rev. B: Condens. Matter Mater. Phys.*, 2015, **91**, 115437.
70 A. S. Rodin, A. Carvalho and A. H. Castro Neto, *Phys. Rev. Lett.*, 2014, **112**, 176801.
71 W. Lei, G. Liu, J. Zhang and M. Liu, *Chem. Soc. Rev.*, 2017, **46**, 3492–3509.
72 R. W. Keyes, *Phys. Rev.*, 1953, **92**, 580.
73 V. Tran and L. Yang, *Phys. Rev. B: Condens. Matter Mater. Phys.*, 2014, **89**, 245407.
74 A. N. Rudenko and M. I. Katsnelson, *Phys. Rev. B: Condens. Matter Mater. Phys.*, 2014, **89**, 201408.
75 S. Zhang, J. Yang, R. Xu, F. Wang, W. Li, M. Ghufran, Y. W. Zhang, Z. Yu, G. Zhang, Q. Qin and Y. Lu, *ACS Nano*, 2014, **8**, 9590–9596.
76 L. Li, J. Kim, C. Jin, G. J. Ye, D. Y. Qiu, F. H. Da Jornada, Z. Shi, L. Chen, Z. Zhang, F. Yang, K. Watanabe, T. Taniguchi, W. Ren, S. G. Louie, X. H. Chen, Y. Zhang and F. Wang, *Nat. Nanotechnol.*, 2017, **12**, 21–25.
77 J. Qiao, X. Kong, Z. X. Hu, F. Yang and W. Ji, *Nat. Commun.*, 2014, **5**, 4475.
78 X. Ling, H. Wang, S. Huang, F. Xia and M. S. Dresselhaus, *Proc. Natl. Acad. Sci. U. S. A.*, 2015, **112**, 4523–4530.
79 H. B. Ribeiro, C. E. P. Villegas, D. A. Bahamon, D. Muraca, A. H. Castro Neto, E. A. T. De Souza, A. R. Rocha, M. A. Pimenta and C. J. S. De Matos, *Nat. Commun.*, 2016, **7**, 12191.
80 Y. Jing, Q. Tang, P. He, Z. Zhou and P. Shen, *Nanotechnology*, 2015, **26**, 095201.
81 C. Zhang, M. Yu, G. Anderson, R. R. Dharmasena and G. Sumanasekera, *Nanotechnology*, 2017, **28**, 075401.
82 R. Fei and L. Yang, *Nano Lett.*, 2014, **14**, 2884–2889.
83 L. Zhou, J. Zhang, Z. Zhuo, L. Kou, W. Ma, B. Shao, A. Du, S. Meng and T. Frauenheim, *J. Phys. Chem. Lett.*, 2016, **7**, 1880–1887.
84 H. Uk Lee, S. C. Lee, J. Won, B. C. Son, S. Choi, Y. Kim, S. Y. Park, H. S. Kim, Y. C. Lee and J. Lee, *Sci. Rep.*, 2015, **5**, 8691.
85 Y. J. Yuan, P. Wang, Z. Li, Y. Wu, W. Bai, Y. Su, J. Guan, S. Wu, J. Zhong, Z. T. Yu and Z. Zou, *Appl. Catal., B*, 2019, **242**, 1–8.
86 Y. Akahama, S. Endo and S. Narita, *J. Phys. Soc. Jpn.*, 1983, **52**, 2148–2155.
87 A. Brown and S. Rundqvist, *Acta Crystallogr.*, 1965, **19**, 684–685.
88 X. Liu, C. R. Ryder, S. A. Wells and M. C. Hersam, *Small Methods*, 2017, 1.
89 H. Yuan, X. Liu, F. Afshinmanesh, W. Li, G. Xu, J. Sun, B. Lian, A. G. Curto, G. Ye, Y. Hikita, Z. Shen, S. C. Zhang, X. Chen, M. Brongersma, H. Y. Hwang and Y. Cui, *Nat. Nanotechnol.*, 2015, **10**, 707–713.
90 X. Ling, S. Huang, E. H. Hasdeo, L. Liang, W. M. Parkin, Y. Tatsumi, A. R. T. Nugraha, A. A. Puretzky, P. M. Das, B. G. Sumpter, D. B. Geohegan, J. Kong, R. Saito, M. Drndic, V. Meunier and M. S. Dresselhaus, *Nano Lett.*, 2016, **16**, 2260–2267.

91 N. Mao, J. Tang, L. Xie, J. Wu, B. Han, J. Lin, S. Deng, W. Ji, H. Xu, K. Liu, L. Tong and J. Zhang, *J. Am. Chem. Soc.*, 2016, **138**, 300–305.
92 F. Xia, H. Wang and Y. Jia, *Nat. Commun.*, 2014, **5**, 4458.
93 J. He, D. He, Y. Wang, Q. Cui, F. Ceballos and H. Zhao, *Nanoscale*, 2015, **7**, 9526–9531.
94 L. Cartz, S. R. Srinivasa, R. J. Riedner, J. D. Jorgensen and T. G. Worlton, *J. Chem. Phys.*, 1979, **71**, 1718–1721.
95 R. Fei, A. Faghaninia, R. Soklaski, J. A. Yan, C. Lo and L. Yang, *Nano Lett.*, 2014, **14**, 6393–6399.
96 A. Jain and A. J. H. McGaughey, *Sci. Rep.*, 2015, **5**, 8501.
97 Z. Luo, J. Maassen, Y. Deng, Y. Du, R. P. Garrelts, M. S. Lundstrom, P. D. Ye and X. Xu, *Nat. Commun.*, 2015, **6**, 8572.
98 S. Lee, F. Yang, J. Suh, S. Yang, Y. Lee, G. Li, H. S. Choe, A. Suslu, Y. Chen, C. Ko, J. Park, K. Liu, J. Li, K. Hippalgaonkar, J. J. Urban, S. Tongay and J. Wu, *Nat. Commun.*, 2015, **6**, 8573.
99 J. Hu, Z. Guo, P. E. McWilliams, J. E. Darges, D. L. Druffel, A. M. Moran and S. C. Warren, *Nano Lett.*, 2016, **16**, 74–79.
100 H. Wang, X. Yang, W. Shao, S. Chen, J. Xie, X. Zhang, J. Wang and Y. Xie, *J. Am. Chem. Soc.*, 2015, **137**, 11376–11382.
101 H. Wang, S. Jiang, W. Shao, X. Zhang, S. Chen, X. Sun, Q. Zhang, Y. Luo and Y. Xie, *J. Am. Chem. Soc.*, 2018, **140**, 3474–3480.
102 L. Pan, X. D. Zhu, K. N. Sun, Y. T. Liu, X. M. Xie and X. Y. Ye, *Nano Energy*, 2016, **30**, 347–354.
103 Z. Yuan, J. Li, M. Yang, Z. Fang, J. Jian, D. Yu, X. Chen and L. Dai, *J. Am. Chem. Soc.*, 2019, **141**, 4972–4979.
104 P. W. Bridgman, *Proc. Natl. Acad. Sci. U. S. A.*, 1937, **23**, 387.
105 I. Shirotani, *Mol. Cryst. Liq. Cryst.*, 1982, **86**, 203–211.
106 L. Q. Sun, M. J. Li, K. Sun, S. H. Yu, R. S. Wang and H. M. Xie, *J. Phys. Chem. C*, 2012, **116**, 14772–14779.
107 C. Lin, L. Yang, L. Ouyang, J. Liu, H. Wang and M. Zhu, *J. Alloys Compd.*, 2017, **728**, 578–584.
108 F. Zhou, L. Ouyang, M. Zeng, J. Liu, H. Wang, H. Shao and M. Zhu, *J. Alloys Compd.*, 2019, **784**, 339–346.
109 D. Zhang, Z. Yuan, G. Zhang, N. Tian, D. Liu and Y. Zhang, *Chin. J. Chem.*, 2018, **76**, 537–542.
110 H. Shin, J. Zhang and W. Lu, *Electrochim. Acta*, 2019, **309**, 264–273.
111 C. M. Park and H. J. Sohn, *Adv. Mater.*, 2007, **19**, 2465–2468.
112 S. Lange, P. Schmidt and T. Nilges, *Inorg. Chem.*, 2007, **46**, 4028–4035.
113 T. Nilges, M. Kersting and T. Pfeifer, *J. Solid State Chem.*, 2008, **181**, 1707–1711.
114 M. Köpf, N. Eckstein, D. Pfister, C. Grotz, I. Krüger, M. Greiwe, T. Hansen, H. Kohlmann and T. Nilges, *J. Cryst. Growth*, 2014, **405**, 6–10.
115 H. Krebs, H. Weitz and K. H. Worms, *Z. Anorg. Allg. Chem.*, 1955, **280**, 119–133.
116 Y. Maruyama, S. Suzuki, K. Kobayashi and S. Tanuma, *Physica B+C*, 1981, **105**, 99–102.
117 M. Baba, F. Izumida, Y. Takeda and A. Morita, *Jpn. J. Appl. Phys.*, 1989, **28**, 1019.
118 H. Liu, A. T. Neal, Z. Zhu, Z. Luo, X. Xu, D. Tománek and P. D. Ye, *ACS Nano*, 2014, **8**, 4033–4041.
119 L. Guan, B. Xing, X. Niu, D. Wang, Y. Yu, S. Zhang, X. Yan, Y. Wang and J. Sha, *Chem. Commun.*, 2018, **54**, 595–598.
120 G. Zhao, T. Wang, Y. Shao, Y. Wu, B. Huang and X. Hao, *Small*, 2017, **7**, 1602243.
121 Z. Huang, H. Hou, Y. Zhang, C. Wang, X. Qiu and X. Ji, *Adv. Mater.*, 2017, **29**, 1702372.
122 A. Ambrosi, Z. Sofer and M. Pumera, *Angew. Chem., Int. Ed.*, 2017, **56**, 10443–10445.
123 J. Li, C. Chen, S. Liu, J. Lu, W. P. Goh, H. Fang, Z. Qiu, B. Tian, Z. Chen, C. Yao, W. Liu, H. Yan, Y. Yu, D. Wang, Y. Wang, M. Lin, C. Su and J. Lu, *Chem. Mater.*, 2018, **30**, 2742–2749.
124 S. Yang, K. Zhang, A. G. Ricciardulli, P. Zhang, Z. Liao, M. R. Lohe, E. Zschech, P. W. M. Blom, W. Pisula, K. Müllen and X. Feng, *Angew. Chem., Int. Ed.*, 2018, **57**, 4677–4681.
125 S. Qiu, B. Zou, H. Sheng, W. Guo, J. Wang, Y. Zhao, W. Wang, R. K. K. Yuen, Y. Kan and Y. Hu, *ACS Appl. Mater. Interfaces*, 2019, **11**, 13652–13664.
126 H. Xiao, M. Zhao, J. Zhang, X. Ma, J. Zhang, T. Hu, T. Tang, J. Jia and H. Wu, *Electrochem. Commun.*, 2018, **89**, 10–13.
127 T. Wang, X. Jin, J. Yang, J. Wu, Q. Yu, Z. Pan, X. Shi, Y. Xu, H. Wu, J. Wang, T. He, K. Zhang and P. Zhou, *ACS Appl. Mater. Interfaces*, 2019, **11**, 36854–36862.
128 L. Zu, X. Gao, H. Lian, C. Li, Q. Liang, Y. Liang, X. Cui, Y. Liu, X. Wang and X. Cui, *J. Alloys Compd.*, 2019, **770**, 26–34.
129 Z. Zhang, X. Xin, Q. Yan, Q. Li, Y. Yang and T.-L. Ren, *Sci. China Mater.*, 2016, **59**, 122–134.
130 J. B. Smith, D. Hagaman and H. F. Ji, *Nanotechnology*, 2016, **27**, 215602.
131 S. Yang, Y. Gong, J. Zhang, L. Zhan, L. Ma, Z. Fang, R. Vajtai, X. Wang and P. M. Ajayan, *Adv. Mater.*, 2013, **25**, 2452–2456.
132 J. N. Coleman, M. Lotya, A. O'Neill, S. D. Bergin, P. J. King, U. Khan, K. Young, A. Gaucher, S. De, R. J. Smith and I. V. Shvets, *Science*, 2011, **331**, 568–571.
133 A. B. Bourlinos, V. Georgakilas, R. Zboril, T. A. Sterioti and A. K. Stubos, *Small*, 2009, **5**, 1841–1845.
134 Z. Guo, H. Zhang, S. Lu, Z. Wang, S. Tang, J. Shao, Z. Sun, H. Xie, H. Wang, X. F. Yu and P. K. Chu, *Adv. Funct. Mater.*, 2015, **25**, 6996–7002.
135 J. Kang, J. D. Wood, S. A. Wells, J. H. Lee, X. Liu, K. S. Chen and M. C. Hersam, *ACS Nano*, 2015, **9**, 3596–3604.
136 P. Yasaei, B. Kumar, T. Foroozan, C. Wang, M. Asadi, D. Tuschel, J. E. Indacochea, R. F. Klie and A. Salehi-Khojin, *Adv. Mater.*, 2015, **27**, 1887–1892.
137 S. Lin, S. Liu, Z. Yang, Y. Li, T. W. Ng, Z. Xu, Q. Bao, J. Hao, C. S. Lee, C. Surya, F. Yan and S. P. Lau, *Adv. Funct. Mater.*, 2016, **26**, 864–871.
138 Y. Zhang, H. Wang, Z. Luo, H. T. Tan, B. Li, S. Sun, Z. Li, Y. Zong, Z. J. Xu, Y. Yang, K. A. Khor and Q. Yan, *Adv. Energy Mater.*, 2016, **12**, 1600453.
139 C. Jia, L. Zhao, M. Cui, F. Yang, G. Cheng, G. Yang and Z. Zeng, *J. Alloys Compd.*, 2019, **799**, 99–107.

140 T. Zhang, Y. Wan, H. Xie, Y. Mu, P. Du, D. Wang, X. Wu, H. Ji and L. Wan, *J. Am. Chem. Soc.*, 2018, **140**, 7561–7567.
141 Z. Zhang, M. Khurram, Z. Sun and Q. Yan, *Inorg. Chem.*, 2018, **57**, 4098–4103.
142 W. Liu, Y. Zhu, Z. Chen, J. Lei and P. Feng, *J. Electron. Mater.*, 2018, **47**, 4793–4798.
143 Z. Yang, J. Hao, S. Yuan, S. Lin, H. M. Yau, J. Dai and S. P. Lau, *Adv. Mater.*, 2015, **27**, 3748–3754.
144 C. Li, Y. Wu, B. Deng, Y. Xie, Q. Guo, S. Yuan, X. Chen, M. Bhuiyan, Z. Wu, K. Watanabe, T. Taniguchi, H. Wang, J. J. Cha, M. Snure, Y. Fei and F. Xia, *Adv. Mater.*, 2018, **30**, 1703748.
145 Y. Zhang, X. Rui, Y. Tang, Y. Liu, J. Wei, S. Chen, W. R. Leow, W. Li, Y. Liu, J. Deng, B. Ma, Q. Yan and X. Chen, *Adv. Energy Mater.*, 2016, **6**, 1502409.
146 B. Tian, B. Tian, B. Smith, M. C. Scott, Q. Lei, R. Hua, Y. Tian and Y. Liu, *Proc. Natl. Acad. Sci. U. S. A.*, 2018, **115**, 4345–4350.
147 X. Zhang, H. Xie, Z. Liu, C. Tan, Z. Luo, H. Li, J. Lin, L. Sun, W. Chen, Z. Xu, L. Xie, W. Huang and H. Zhang, *Angew. Chem., Int. Ed.*, 2015, **54**, 3653–3657.
148 Z. Sun, H. Xie, S. Tang, X. Yu, Z. Guo, J. Shao, H. Zhang, H. Huang, H. Wang and P. K. Chu, *Am. Ethnol.*, 2015, **127**, 11688–11692.
149 L. F. Gao, J. Y. Xu, Z. Y. Zhu, C. X. Hu, L. Zhang, Q. Wang and H. L. Zhang, *Nanoscale*, 2016, **8**, 15132–15136.
150 W. Chen, K. Li, Y. Wang, X. Feng, Z. Liao, Q. Su, X. Lin and Z. He, *J. Phys. Chem. Lett.*, 2017, **8**, 591–598.
151 X. Tang, H. Chen, J. S. Ponraj, S. C. Dhanabalan, Q. Xiao, D. Fan and H. Zhang, *Adv. Sci.*, 2018, **5**, 1800420.
152 C. Zhu, F. Xu, L. Zhang, M. Li, J. Chen, S. Xu, G. Huang, W. Chen and L. Sun, *Chem. – Eur. J.*, 2016, **22**, 7357–7362.
153 Y. Xu, Z. Wang, Z. Guo, H. Huang, Q. Xiao, H. Zhang and X. F. Yu, *Adv. Opt. Mater.*, 2016, **4**, 1223–1229.
154 W. Gu, X. Pei, Y. Cheng, C. Zhang, J. Zhang, Y. Yan, C. Ding and Y. Xian, *ACS Sens.*, 2017, **2**, 576–582.
155 Q. Zhang, J. Zhang, L. Zhang, M. Cao, F. Yang and W. L. Dai, *Appl. Surf. Sci.*, 2020, **504**, 144366.
156 Q. Zhang, S. Huang, J. Deng, D. T. Gangadharan, F. Yang, Z. Xu, G. Giorgi, M. Palummo, M. Chaker and D. Ma, *Adv. Funct. Mater.*, 2019, **29**, 1902486.
157 R. Gui, H. Jin, Z. Wang and J. Li, *Chem. Soc. Rev.*, 2018, **47**, 6795–6823.
158 L. Kong, Y. Ji, Z. Dang, J. Yan, P. Li, Y. Li and S. F. Liu, *Adv. Funct. Mater.*, 2018, **28**, 1800668.
159 K. L. Utt, P. Rivero, M. Mehboudi, E. O. Harriss, M. F. Borunda, A. A. P. San Juan and S. Barraza-Lopez, *ACS Cent. Sci.*, 2015, **1**, 320–327.
160 A. Favron, E. Gaufrès, F. Fossard, A. L. Phaneuf-Laheureux, N. Y. W. Tang, P. L. Lévesque, A. Loiseau, R. Leonelli, S. Francoeur and R. Martel, *Nat. Mater.*, 2015, **14**, 826–832.
161 K. L. Kuntz, R. A. Wells, J. Hu, T. Yang, B. Dong, H. Guo, A. H. Woomer, D. L. Druffel, A. Alabanza, D. Tománek and S. C. Warren, *ACS Appl. Mater. Interfaces*, 2017, **9**, 9126–9135.
162 D. K. Sang, H. Wang, Z. Guo, N. Xie and H. Zhang, *Adv. Funct. Mater.*, 2019, **29**, 1903419.
163 C. R. Ryder, J. D. Wood, S. A. Wells, Y. Yang, D. Jariwala, T. J. Marks, G. C. Schatz and M. C. Hersam, *Nat. Chem.*, 2016, **8**, 597–602.
164 G. Abellán, V. Lloret, U. Mundloch, M. Marcia, C. Neiss, A. Görling, M. Varela, F. Hauke and A. Hirsch, *Angew. Chem., Int. Ed.*, 2016, **55**, 14557–14562.
165 Y. Zhao, H. Wang, H. Huang, Q. Xiao, Y. Xu, Z. Guo, H. Xie, J. Shao, Z. Sun, W. Han, X. Yu, P. Li and P. K. Chu, *Am. Ethnol.*, 2016, **128**, 5087–5091.
166 W. Lei, T. Zhang, P. Liu, J. A. Rodriguez, G. Liu and M. Liu, *ACS Catal.*, 2016, **6**, 8009–8020.
167 L. Bai, X. Wang, S. Tang, Y. Kang, J. Wang, Y. Yu, Z. K. Zhou, C. Ma, X. Zhang, J. Jiang, P. K. Chu and X. F. Yu, *Adv. Mater.*, 2018, **30**, 1803641.
168 İ. Aksoy, H. Küçükkeçeci, F. Sevgi, Ö. Metin and I. Hatay Patir, *ACS Appl. Mater. Interfaces*, 2020, **12**, 26822–26831.
169 Z. K. Shen, M. Cheng, Y. J. Yuan, L. Pei, J. Zhong, J. Guan, X. Li, Z. J. Li, L. Bao, X. Zhang, Z. T. Yu and Z. Zou, *Appl. Catal., B*, 2021, **295**, 120274.
170 Y. J. Yuan, Z. K. Shen, S. Song, J. Guan, L. Bao, L. Pei, Y. Su, S. Wu, W. Bai, Z. T. Yu, Z. Ji and Z. Zou, *ACS Catal.*, 2019, **9**, 7801–7807.
171 X. Zhu, G. Zhou, J. Yi, P. Ding, J. Yang, K. Zhong, Y. Song, Y. Hua, X. Zhu, J. Yuan, Y. She, H. Li and H. Xu, *ACS Appl. Mater. Interfaces*, 2021, **13**, 39523–39532.
172 J. Hu, T. Yang, X. Yang, J. Qu, Y. Cai and C. M. Li, *Small*, 2022, **18**, 2105376.
173 M. Bühl and A. Hirsch, *Chem. Rev.*, 2001, **101**, 1153–1183.
174 J. C. Scanlon, J. M. Brown and L. B. Ebert', *J. Phys. Chem.*, 1994, **98**, 3921–3923.
175 P. Jodie, L. Conyers and J. L. Conyers, *Int. J. Nanomedicine*, 2009, 261–275, DOI: **10.2147/ijn.s5964**.
176 X. Dong, Z. Xin, D. He, J. L. Zhang, Y. Q. Lan, Q. F. Zhang and Y. Chen, *Chin. Chem. Lett.*, 2023, **34**, 107459.
177 W. Wang, Y. Tao, J. Fan, Z. Yan, H. Shang, D. L. Phillips, M. Chen and G. Li, *Adv. Funct. Mater.*, 2022, **32**, 2201357.
178 X. Zhu, T. Zhang, D. Jiang, H. Duan, Z. Sun, M. Zhang, H. Jin, R. Guan, Y. Liu, M. Chen, H. Ji, P. Du, W. Yan, S. Wei, Y. Lu and S. Yang, *Nat. Commun.*, 2018, **9**, 4177.
179 Z. Zhang, D. He, H. Liu, M. Ren, Y. Zhang, J. Qu, N. Lu, J. Guan and X. Yuan, *Environ. Pollut.*, 2019, **245**, 950–956.
180 K. Ge, Y. Zhang, D. Wang, Z. Li, J. He, C. Fu, Y. Yang, M. Pan and L. Zhu, *ACS Appl. Mater. Interfaces*, 2020, **12**, 20035–20043.
181 H. Cai, B. Wang, L. Xiong, J. Bi, L. Yuan, G. Yang and S. Yang, *Appl. Catal., B*, 2019, **256**, 117853.
182 A. J. Bard, *J. Photochem.*, 1979, **10**, 59–75.
183 G. Di, Z. Zhu, H. Zhang, J. Zhu, Y. Qiu, D. Yin and S. Küppers, *J. Colloid Interface Sci.*, 2019, **538**, 256–266.
184 Z. Qin, W. Fang, J. Liu, Z. Wei, Z. Jiang and W. Shangguan, *Cuihua Xuebao*, 2018, **39**, 472–478.
185 Y. R. Lin, G. V. C. Dizon, K. Yamada, C. Y. Liu, A. Venault, H. Y. Lin, M. Yoshida and C. Hu, *J. Colloid Interface Sci.*, 2020, **567**, 202–212.
186 Y. Sasaki, H. Kato and A. Kudo, *J. Am. Chem. Soc.*, 2013, **135**, 5441–5449.

187 Y. Gong, X. Quan, H. Yu, S. Chen and H. Zhao, *Appl. Catal., B*, 2018, **237**, 947–956.
188 R. Abe, K. Sayama, K. Domen and H. Arakawa, *Chem. Phys. Lett.*, 2001, **344**, 339–344.
189 P. Zhou, J. Yu and M. Jaroniec, *Adv. Mater.*, 2014, **26**, 4920–4935.
190 X. Xia, M. Song, H. Wang, X. Zhang, N. Sui, Q. Zhang, V. L. Colvin and W. W. Yu, *Nanoscale*, 2019, **11**, 11071–11082.
191 L. Jiang, X. Yuan, G. Zeng, J. Liang, Z. Wu and H. Wang, *Environ. Sci.: Nano*, 2018, **5**, 599–615.
192 H. Tada, T. Mitsui, T. Kiyonaga, T. Akita and K. Tanaka, *Nat. Mater.*, 2006, **5**, 782–786.
193 W. Xue, D. Huang, X. Wen, S. Chen, M. Cheng, R. Deng, B. Li, Y. Yang and X. Liu, *J. Hazard. Mater.*, 2020, **390**, 121218.
194 A. Iwase, Y. H. Ng, Y. Ishiguro, A. Kudo and R. Amal, *J. Am. Chem. Soc.*, 2011, **133**, 11054–11057.
195 K. E. Byun, H. J. Chung, J. Lee, H. Yang, H. J. Song, J. Heo, D. H. Seo, S. Park, S. W. Hwang, I. Yoo and K. Kim, *Nano Lett.*, 2013, **13**, 4001–4005.
196 Q. Xu, L. Zhang, J. Yu, S. Wageh, A. A. Al-Ghamdi and M. Jaroniec, *Mater. Today*, 2018, **21**, 1042–1063.
197 W. Jiang, W. Luo, J. Wang, M. Zhang and Y. Zhu, *J. Photochem. Photobiol., C*, 2016, **28**, 87–115.
198 X. Wang, G. Liu, Z. G. Chen, F. Li, L. Wang, G. Q. Lu and H. M. Cheng, *Chem. Commun.*, 2009, 3452–3454.
199 M. Zhu, Z. Sun, M. Fujitsuka and T. Majima, *Angew. Chem., Int. Ed.*, 2018, **57**, 2160–2164.
200 J. Hu, D. Chen, Z. Mo, N. Li, Q. Xu, H. Li, J. He, H. Xu and J. Lu, *Angew. Chem., Int. Ed.*, 2019, **58**, 2073–2077.
201 F. Liu, R. Shi, Z. Wang, Y. Weng, C. M. Che and Y. Chen, *Angew. Chem., Int. Ed.*, 2019, **58**, 11791–11795.
202 R. Shi, F. Liu, Z. Wang, Y. Weng and Y. Chen, *Chem. Commun.*, 2019, **55**, 12531–12534.
203 Y. Zhang, L. Wang, S. H. Park, X. Kong, X. Lan, Z. Song and J. Shi, *Chem. Eng. J.*, 2019, **375**, 121967.
204 S. Xu, S. Gong, H. Jiang, P. Shi, J. Fan, Q. J. Xu and Y. L. Min, *Appl. Catal., B*, 2020, **267**, 118661.
205 L. Wang, R. Guan, Y. Qi, F. Zhang, P. Li, J. Wang, P. Qu, G. Zhou and W. Shi, *J. Colloid Interface Sci.*, 2021, **600**, 463–472.
206 M. Wang, D. Li, Y. Zhao, H. Shen, B. Chen, X. Wu, X. Qiao and W. Shi, *Catal. Sci. Technol.*, 2021, **11**, 681–688.
207 M. Hu, J. Zhu, W. Guo, Q. Xu, Y. Min and J. Fan, *ACS Sustainable Chem. Eng.*, 2022, **10**, 1008–1019.